

Tidal Response of Mars Constrained from Laboratory-based Viscoelastic Dissipation Models and Geophysical Data

A. Bagheri¹, A. Khan^{2,1}, D. Al-Attar³, O. Crawford³, D. Giardini¹

¹Institute of Geophysics, ETH Zürich, Zürich, Switzerland

²Institute of Theoretical Physics, University of Zürich, Zürich, Switzerland

³Bullard Laboratories, Department of Earth Sciences, University of Cambridge, Cambridge, UK

Key Points:

- We present a method for determining the planetary tidal response using laboratory-based viscoelastic models and apply it to Mars.
- Maxwellian rheology results in considerably biased (low) viscosities and should be used with caution when studying tidal dissipation.
- Mars' rheology and interior structure will be further constrained from InSight measurements of tidal phase lags at distinct periods.

Abstract

We employ laboratory-based grain-size- and temperature-sensitive rheological models to describe the viscoelastic behavior of terrestrial bodies with focus on Mars. Shear modulus reduction and attenuation related to viscoelastic relaxation occur as a result of diffusion- and dislocation-related creep and grain-boundary processes. We consider five rheological models, including extended Burgers, Andrade, Sundberg-Cooper, a power-law approximation, and Maxwell, and determine Martian tidal response. However, the question of which model provides the most appropriate description of dissipation in planetary bodies, remains an open issue. To examine this, crust and mantle models (density and elasticity) are computed self-consistently through phase equilibrium calculations as a function of pressure, temperature, and bulk composition, whereas core properties are based on an Fe-FeS parameterisation. We assess the compatibility of the viscoelastic models by inverting the available geophysical data for Mars (tidal response and mean density and moment of inertia) for temperature, elastic, and attenuation structure. Our results show that although all viscoelastic models are consistent with data, their predictions for the tidal response at other periods and harmonic degrees are distinct. The results also show that Maxwell is only capable of fitting data for unrealistically low viscosities. Our approach can be used quantitatively to distinguish between the viscoelastic models from seismic and/or tidal observations that will allow for improved constraints on interior structure (e.g., with InSight). Finally, the methodology presented here is generally formulated and applicable to other solar and extra-solar system bodies where the study of tidal dissipation presents an important means for determining interior structure.

36 **Plain Language Summary**

37 A planet responds to external tidal forces, such as those created by an orbiting moon,
38 by deforming, which causes a change in its external gravitational potential field. If the
39 body responds elastically, the tide raised on the planet by its moon will be aligned with
40 the tide-raising potential as a result of which there will be no dissipation of energy within
41 the planet. However, ordinary planetary materials respond anelastically, which means that
42 energy is being dissipated and, consequently, the tidal bulge will be misaligned with the
43 tide-raising moon. The amount by which a planetary body responds to an external tidal
44 force depends on its interior structure such that rigid bodies will not deform appreciably,
45 whereas less rigid bodies can deform significantly. Here, we use this observation for the
46 Mars-Phobos system to constrain the interior structure of Mars. The models that describe
47 the planet's response to an external force are based on laboratory measurements of the de-
48 formation of major planetary materials. The Mars InSight mission will make further mea-
49 surements of the tidal response of Mars for comparison with our modeling results, which
50 will improve our understanding of Mars's interior structure and dynamical evolution.

1 Introduction

A planet responds to tidal forces by deforming, which causes a change in its gravitational potential field (see Figure 1). If the response is purely elastic, the tide raised on the planet by its moon, and vice versa, will be aligned with the tide-raising potential as a result of which the orbit of the moon will be unaffected, i.e., there is no torque acting and no dissipation occurs within either body. If, however, the planet reacts anelastically, dissipation is acting, as a result of which the tidal bulge and the tide-raising potential are misaligned. Since the tidal bulge reacts by applying a torque, which is proportional to the amplitude of the tide and to the sine of the tidal lag angle or phase lag, the orbit of the moon changes. Consequently, the phase lag is a measure of tidal dissipation and is determined from the angle between the tide-raising force and the tide itself and depends on the anelastic structure, whereas the amplitude of the tidal response is mostly sensitive to the elastic structure. Thus by measuring orbital changes of natural or artificial satellites around planets or landed spacecraft, information on a planet's interior structure can be derived as has been done for the terrestrial solar system planets and the Moon [e.g., *Padovan et al.*, 2013; *Efroimsky and Lainey*, 2007; *Hauck et al.*, 2013; *Yoder*, 1995; *Konopliv and Yoder*, 1996; *Rivoldini et al.*, 2011; *Bills et al.*, 2005; *Khan and Connolly*, 2008; *Williams et al.*, 2006; *Nimmo et al.*, 2012; *Nimmo and Faul*, 2013; *Dumoulin et al.*, 2017; *Williams et al.*, 2014; *Williams and Boggs*, 2015; *Khan et al.*, 2018; *Zharkov and Gudkova*, 2005; *Yoder et al.*, 2003, among others].

The anelastic processes that most solid state materials undergo in response to a forcing are governed by dissipative processes at the microscopic scale, in particular viscoelastic relaxation of the shear modulus due to elastically-accommodated, and dislocation- and diffusion-assisted grain-boundary sliding [*Karato and Spetzler*, 1990; *Ranalli*, 2001; *Takei et al.*, 2014; *Faul and Jackson*, 2015; *Karato et al.*, 2015]. Several models have been proposed to describe the viscoelastic behavior of planetary materials. For example, Maxwell's model, the simplest of all rheological models, has often been called upon when studying tidal dissipation in planets and moons [e.g., *Bills et al.*, 2005; *Correia et al.*, 2014; *Remus et al.*, 2012; *Efroimsky and Lainey*, 2007]. Yet this model only includes an elastic and a viscous response without a transient regime that, from a time-scale point of view, covers most of the period range of interest where tidal dissipation actually occurs. Also, Maxwell's model has difficulty in reproducing the observed frequency dependence of dissipation $\propto \omega^{-\alpha}$, where ω is angular frequency and α the frequency exponent [e.g., *Minster*

84 *and Anderson, 1981; Jackson et al., 2002; Benjamin et al., 2006; Jackson and Faul, 2010*].
 85 As a consequence, Maxwellian rheology results in an unsatisfactory explanation for the
 86 tidal response of planetary bodies like Mars, the Moon, and the Earth [*Bills et al., 2005;*
 87 *Nimmo et al., 2012; Nimmo and Faul, 2013; Williams and Boggs, 2015; Renaud and Hen-*
 88 *ning, 2018; Lau and Faul, 2019*].

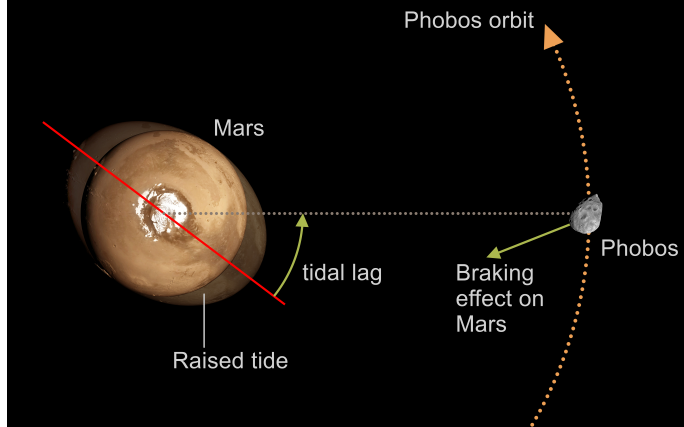
89 In response hereto, more complex grain-size- and temperature-dependent models
 90 have been proposed. Among these figure the models of Andrade, Burgers, Sundberg-
 91 Cooper, and power-law approximation scheme, which have been studied experimentally
 92 [*Jackson et al., 2002; Sundberg and Cooper, 2010; Jackson and Faul, 2010; Takei et al.,*
 93 *2014; McCarthy et al., 2011; Sasaki et al., 2019*]. Laboratory experiments of torsional
 94 forced oscillation data on anhydrous melt-free olivine appear to favour the extended Burg-
 95 ers model over other rheological models because of its ability to describe the transition
 96 from (anharmonic) elasticity to grain size-sensitive viscoelastic behaviour [*Faul and Jack-*
 97 *son, 2015*]. Because of the improved flexibility that comes with a larger number of de-
 98 grees of freedom, application of these laboratory-based dissipation models to geophysical
 99 problems has nonetheless resulted in considerable improvement in matching the observed
 100 frequency dependence of dissipation, in addition to simultaneously fitting attenuation-
 101 related data that span the frequency range from the dominant seismic wave period (~ 1 s)
 102 over normal modes (~ 1 hour) to the very long-period tides (~ 20 years), i.e., a frequency
 103 range spanning 5 orders of magnitude [*Henning et al., 2009; Efroimsky, 2012a,b; Nimmo*
 104 *et al., 2012; Nimmo and Faul, 2013; Khan et al., 2018; Lau and Faul, 2019; Benjamin*
 105 *et al., 2006; Renaud and Henning, 2018*].

106 While qualitatively similar in that the various viscoelastic models can be described
 107 in terms of dashpot and spring elements that are arranged in series and parallel, it is yet to
 108 be understood to what extent these models are quantitatively similar on planetary scales,
 109 i.e., are capable of making predictions that match global geophysical observations at dif-
 110 ferent forcing frequencies for a set of realistic models of the interior structure of planets.
 111 While most studies focus on application of a single viscoelastic dissipation model to so-
 112 lar system objects: Mercury [*Padovan et al., 2013*], Venus [*Dumoulin et al., 2017*], Earth
 113 [*Bellis and Holtzman, 2014; Abers et al., 2014; Agnew, 2015; Karato et al., 2015; Lau and*
 114 *Faul, 2019*], the Moon [*Nimmo et al., 2012; Efroimsky, 2012a,b; Karato, 2013; Harada*
 115 *et al., 2014; Williams and Boggs, 2015; Qin et al., 2016*], Mars [*Lognonné and Mosser,*
 116 *1993; Yoder et al., 2003; Sohl et al., 2005; Zharkov and Gudkova, 2005; Bills et al., 2005;*

117 *Efroimsky and Lainey, 2007; Nimmo and Faul, 2013; Khan et al., 2018*], Io [*Hussmann*
 118 *and Spohn, 2004; Bierson and Nimmo, 2016; Renaud and Henning, 2018*], Iapetus [*Peale,*
 119 *1977; Robuchon et al., 2010; Castillo-Rogez et al., 2011*], Europa [*Moore and Schubert,*
 120 *2000; Hussmann and Spohn, 2004; Wahr et al., 2009; A et al., 2014*], Ganymede [*A et al.,*
 121 *2014; Kamata et al., 2016*], Enceladus [*Roberts and Nimmo, 2008; Choblet et al., 2017*],
 122 and exoplanets [*Henning et al., 2009; Efroimsky, 2012b; Renaud and Henning, 2018*], stud-
 123 ies that quantitatively investigate several viscoelastic models concomitantly by formulating
 124 the problem in a geophysical inverse sense have yet to be undertaken.

125 With this in mind, we consider a series of laboratory-based viscoelastic dissipa-
 126 tion models and quantitatively compare them using geophysical inversion with the pur-
 127 pose of constraining attenuation properties of planets from seismic to tidal time scales.
 128 Here, we focus on Mars for which the tidal response due to Phobos (amplitude and phase
 129 lag), in addition to mean density and mean moment of inertia, are available. The approach
 130 adopted here builds upon and extends previous work [e.g., *Renaud and Henning, 2018;*
 131 *Khan et al., 2018*] in that it seeks to combine a suite of experimentally-constrained grain
 132 size-, temperature- and frequency-dependent viscoelastic models (Andrade, extended Burg-
 133 ers, Sundberg-Cooper, Maxwell, and a power-law approximation scheme) with petrologic
 134 phase equilibrium computations that enables self-consistent computation of geophysical
 135 responses for direct comparison to observations. The advantage of this approach is that it
 136 anchors internal structure parameters that are in laboratory-based models, while geophys-
 137 ical inverse methods are simultaneously employed to optimise profiles of e.g., seismic wave
 138 speeds, dissipation, and density to match a set of geophysical observations.

139 Quantitative predictions of e.g., the tidal response at different periods can be made
 140 and tested against results that are expected to be obtained from the Mars InSight (Interior
 141 Exploration using Seismic Investigations, Geodesy and Heat Transport) mission, which
 142 has been operating on Mars for eight months since its deployment. InSight will measure
 143 attenuation, with both the SEIS (Seismic Experiment for Internal Structure) [*Lognonné,*
 144 *2019*] and RISE (Rotation and Interior Structure Experiment) [*Folkner et al., 2018*] in-
 145 struments at periods ranging from seconds (seismic events) to months (nutation and pre-
 146 cession of Mars's rotation axis). The observation of attenuation at periods other than
 147 the main Phobos tide provides a means for distinguishing between the various laboratory-
 148 based dissipation models and will turn out to be of particular importance for understand-
 149 ing the thermal and viscoelastic behaviour of Mars. For community use, we tabulated pre-



157 **Figure 1.** Illustration of the tidal interaction between Mars and its larger moon Phobos. Courtesy of David
 158 Ducros/IPGP.

150 dicted model responses (Love numbers and attenuation) at a number of distinct periods
 151 and spherical harmonic degree for each of the rheological models considered here. Fi-
 152 nally, we would like to note that although this study focuses on Mars, the methodology
 153 described herein is generally applicable and is easily extendable to other solar system bod-
 154 ies and beyond.

155 2 Background

156 2.1 Geophysical Analysis

159 The tidal bulge raised on Mars (see Figure 1) due to its orbiting moons Phobos and
 160 Deimos, is a function of its internal structure and the forcing itself. Because dissipation
 161 is acting, the bulge does not align with the barycentric axis (defined as the line that ex-
 162 tends between the center of masses of the two objects and indicated by the dashed line
 163 in Figure 1) but is lagging behind Phobos and ahead of Deimos. As a result of the tidal
 164 bulge, changes in the potential field and deformations in both radial and tangential direc-
 165 tions of Mars ensue (the same holds for the moons). The change in the potential field of a
 166 planet of radius r , subjected to a perturbation in potential Φ due to an orbiting moon is
 167 denoted by ϕ , and can be expressed as a spherical harmonics expansion in time domain as
 168 (in what follows we rely on the formulation of *Efroimsky and Makarov* [2014])

$$\phi_n(R, t) = k_n \left(\frac{R}{r} \right)^{n+1} \Phi_n(R, R^*), \quad (1)$$

169 where n indicates the spherical harmonic degree, k_n is the potential Love operator of de-
 170 gree n , R^* is the position of the perturbing body, and R is a point on Mars's surface. The
 171 displacement Love operators, h_n and l_n express the resultant vertical (radial) and hori-
 172 zontal (tangential) displacements at the surface of the planet as $h_n\Phi_n/g$ and $l_n\nabla\Phi_n/g$,
 173 respectively, where g is the gravitational acceleration at the surface. In addition to the
 174 Love numbers, the magnitude of the change in gravity due to the change in the poten-
 175 tial field is of interest. This parameter, the gravimetric factor δ , is computed as $\delta_n =$
 176 $1 + 2h_n/n - k_n(n + 1/n)$ [e.g., *Agnew, 2015*].

177 In the frequency domain, equation 1 can be written as

$$\phi_n(R, \omega_{pq}^{nm}) = \left(\frac{R}{r}\right)^{n+1} \bar{k}_n(\omega_{pq}^{nm}) \bar{\Phi}_n(R, R^*, \omega_{pq}^{nm}), \quad (2)$$

178 where, ω_{pq}^{nm} are the Fourier tidal modes, nm and pq are integers used to number the modes,
 179 and \bar{k}_n is the complex frequency-dependent Love number where $\bar{k}_n(\omega_{pq}^{nm}) = \Re[\bar{k}_n(\omega_{pq}^{nm})] +$
 180 $i\Im[\bar{k}_n(\omega_{pq}^{nm})]$. The Love number k_n can be written as $|\bar{k}_n| \exp(-i\epsilon_n)$, where ϵ_n is the phase
 181 angle between the tidal force and resulting bulge and equals the geometric lag (δ_{pq}^{nm}) (la-
 182 beled "tidal lag" in Figure 1) through $\delta_{pq}^{nm} = \epsilon_{pq}^{nm}/m$ [e.g., *Efroimsky and Makarov, 2013*].
 183 The phase angle is also related to the energy that is being dissipated in the tides as $1/Q_n$,
 184 where Q_n is the tidal quality factor of spherical harmonic degree n

$$Q_n = \frac{1}{\sin|\epsilon_n|} = \frac{\sqrt{\Re^2(k_n) + \Im^2(k_n)}}{|\Im(k_n)|}, \quad (3)$$

185 For the terrestrial planets, ϵ_n is usually small at the main tidal periods (except when the
 186 satellite is very close to the resonance period), as a result of which Q_n can be approxi-
 187 mated by

$$Q_n \approx \frac{1}{\tan|\epsilon_n|} = \frac{\Re(k_n)}{|\Im(k_n)|}. \quad (4)$$

188 In the following section, we turn our attention to intrinsic shear attenuation.

189 2.2 Viscoelastic Dissipation Models

190 While elasticity is a result of bond stretching along crystallographic planes in an
 191 ordered solid, viscosity and dissipation inside a polycrystalline material occur by mo-
 192 tion of point, linear, and planar defects, facilitated by diffusion. In viscoelastic behavior,
 193 each of these mechanisms contribute [e.g., *Karato, 2008*]. Deformations of a viscoelas-
 194 tic solid depends on the temporal-scale of the applied load [*Chawla and Meyers, 1999*].
 195 For small stresses, the stress-strain relation is linear, and the response is described in the

196 time-domain via the creep function $J(t)$. The creep function links material properties and
 197 forcing (input) with the “felt” (relaxed) shear modulus and phase lag due to attenuation
 198 (output). The response of the material to forcing consists of an instantaneous elastic re-
 199 sponse followed by a semi-recoverable transient flow regime where the strain rate changes
 200 with time, and finally yields to steady-state creep. Based on this, the general form of the
 201 creep function for a viscoelastic solid consists of three terms:

$$\underbrace{J(t)}_{\text{Creep function}} = \underbrace{J_U}_{\text{Elastic}} + \underbrace{f(t)}_{\text{Transient strain-rate}} + \underbrace{t/\eta}_{\text{Viscous}}, \quad (5)$$

202 where t is time and η is the steady-state Newtonian viscosity. The complex shear modulus
 203 \hat{G} is computed from the Laplace-transformed creep or the complex compliance $\hat{J} = \Re(\hat{J}) +$
 204 $i\Im(\hat{J})$ through $\hat{G} = 1/\hat{J}$ [Findley and Onaran, 1965]. The relaxed shear modulus and the
 205 associated dissipation (Q_μ^{-1}) are obtained from the following expressions:

$$G_R(\omega) = \{\Re^2[\hat{J}(\omega)] + \Im^2[\hat{J}(\omega)]\}^{-\frac{1}{2}}, \quad (6)$$

207

$$Q_\mu^{-1} \approx |\Im[\hat{J}(\omega)]|/\Re[\hat{J}(\omega)]. \quad (7)$$

208 Note that Q_μ is an intrinsic material property and therefore different from the global Q_n
 209 discussed in the previous section (cf. Eq. 3). Briefly, and as discussed in more detail in
 210 e.g., *Efroimsky* [2015] and *Lau et al.* [2016], the distinction between global tidal dissipa-
 211 tion (Q_n) and intrinsic attenuation (Q_μ), which is a spatially-varying material property and
 212 responsible for the attenuation of e.g., seismic waves, derives from the fact that Q_n , in ad-
 213 dition to “sensing” Q_μ , is also influenced by gravity and inertial effects due to rotation
 214 of the planet. At reasonably high frequencies, this distinction becomes redundant as Q_n
 215 approaches Q_μ .

216 In the following, we consider a suite of laboratory-based viscoelastic dissipation
 217 models: Maxwell, extended Burgers, Andrade, Sundberg-Cooper, and a power-law scheme.
 218 These models derive from grain-size, temperature-, and pressure-sensitive viscoelastic re-
 219 laxation measurements. The dissipation models based on Maxwell, extended Burgers, An-
 220 drade, and the power-law scheme are described in detail in *Jackson and Faul* [2010] and
 221 rely on laboratory experiments (temperature range 800–1200°C) of torsional forced os-
 222 cillation data (period range 1–1000 s) on melt-free poly-crystalline olivine (grain sizes
 223 in the range 3–165 μm). The model of Sundberg and Cooper [Sundberg and Cooper,
 224 2010] is also based on torsional oscillation data, but in a fine-grained (5 μm) peridotite

(olivine+39 vol% orthopyroxene) specimen (temperature range 1200–1300°C and periods of 1–~200 s).

As shown in figure 2, each model can be represented as an arrangement of springs and dashpots connected in series, or in parallel, or a combination of both [Findley and Onaran, 1965; Moczo and Kristek, 2005; Nowick and Berry, 1972; Cooper, 2002; Jackson et al., 2007; McCarthy and Castillo-Rogez, 2013]. The instantaneous elastic response is mimicked by a spring (element 1, E1) and the fully viscous behavior by that of a dashpot (element 2, E2). The series connection (i.e., a Maxwell module), includes a non-recoverable displacement, while a parallel connection (a Voigt module) ensures fully recoverable deformations with either a discrete (element 3, E3) or a continuous distribution (element 4, E4, henceforth “modified” Voigt module) of anelastic relaxation times. These models have been applied in various circumstances to model the response of planetary bodies. In the following, we briefly describe each of these models that are employed later to model tidal dissipation within Mars.

2.2.1 Maxwell

Maxwell is the simplest model for expressing the viscoelastic behavior and is a series connection of a spring and dashpot. The associated creep function with this model is:

$$J(t) = \underbrace{J_U}_{E1} + \underbrace{\frac{t}{\eta}}_{E2}. \quad (8)$$

Here, J_U is the unrelaxed, i.e., infinite-frequency, compliance, and E1 and E2 represent spring and dashpot elements (cf. Figure 2), respectively. The compliance for this model is

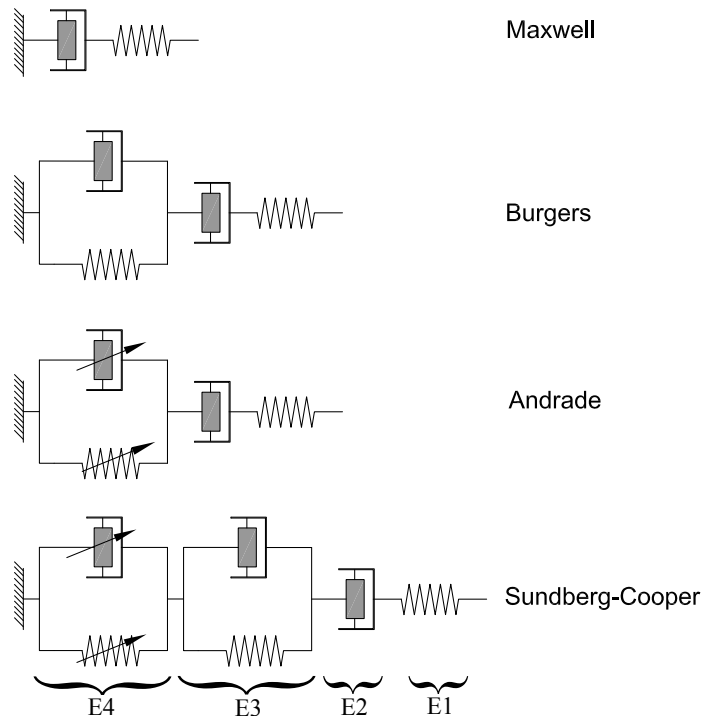
$$\hat{J} = J_U - \frac{i}{\omega}, \quad (9)$$

and real and imaginary parts of the complex shear modulus are computed from equation 6

$$\Re[\hat{G}(\omega)] = \frac{\tau_M^2 \omega^2}{J_U(\tau_M^2 \omega^2 + 1)}, \quad (10)$$

$$\Im[\hat{G}(\omega)] = \frac{\tau_M \omega}{J_U(\tau_M^2 \omega^2 + 1)}, \quad (11)$$

where $\tau_M = \eta/G_U$ is the Maxwell time, ω is frequency, and G_U is the unrelaxed shear modulus. As is apparent from comparison of equations 6 and 8, this model does not include a transient phase and immediately drops to the viscous fluid regime from the elastic response. Hence, while this model represents a reasonable approximation for very



239 **Figure 2.** Schematic representation of the viscoelastic models in terms of springs and dashpots. A spring
 240 element (E1) represents a purely elastic response, whereas a dashpot element (E2) is representative of purely
 241 viscous damping. A series connection of elements 1 and 2 is representative of the response of a Maxwell
 242 model (irrecoverable), whereas a connection of elements 1 and 2 in parallel (element 3) results in an anelastic
 243 (recoverable) response with a discrete (single) spectrum of relaxation times. Arrows on spring and dashpot in
 244 element 4, conversely, indicate an element that incorporates a continuous distribution of anelastic relaxation
 245 times and results in a broadened response spectrum. Modified from *Renaud and Henning* [2018].

259 long-period loading such as glacial isostatic adjustments [Peltier, 1974], it does not suf-
 260 fice for modeling the viscoelastic behaviour at intermediate periods. An extended form of
 261 Maxwell's model is employed in this study, where effects of grain size, temperature, and
 262 pressure are accounted for through a modification of the Maxwell time (τ_M) [e.g., Morris
 263 and Jackson, 2009; Jackson and Faul, 2010; McCarthy et al., 2011] according to

$$\tau_M(T, P, d) = \tau_{M0} \left(\frac{d_g}{d_0} \right)^{m_{gv}} \exp \left[\left(\frac{E^*}{R} \right) \left(\frac{1}{T} - \frac{1}{T_0} \right) \right] \exp \left[\left(\frac{V^*}{R} \right) \left(\frac{P}{T} - \frac{P_0}{T_0} \right) \right], \quad (12)$$

264 where R is the gas constant, E^* is activation energy, V^* is activation volume, m_{gv} is grain
 265 size exponent for viscous relaxation, P is pressure, T is temperature, and τ_{M0} is a normal-
 266 ized value at a particular set of reference conditions (d_0 , P_0 , and T_0). Parameter values
 267 used here and in the following are tabulated in Table A.1.

268 2.2.2 Extended Burgers

269 The shortcoming of Maxwell's model in representing a transient response between
 270 elastic and viscous regimes can be rectified by introducing a time-dependent anelastic
 271 transition between these two regimes. This implies connecting a Voigt module (E3) and
 272 a Maxwell module (E1 and E2 connected in series) as shown in Figure 2. For this model,
 273 the creep function takes the form

$$J(t) = \underbrace{J_U}_{E1} + \underbrace{\Delta J \left[1 - \exp \left(-\frac{t}{\tau} \right) \right]}_{E3} + \underbrace{\frac{t}{\eta}}_{E2}, \quad (13)$$

274 where E3 corresponds to the anelastic time-dependent response, J_U is, as before, unre-
 275 laxated compliance, respectively, ΔJ is the magnitude of the anelastic contribution, and τ is
 276 the time constant for the development of the anelastic response. More generally, the sin-
 277 gular anelastic relaxation time τ can be replaced by a distribution $D(\tau)$ of relaxation times
 278 over an interval specified by upper (τ_H) and lower bounds (τ_L) [Jackson and Faul, 2010].
 279 From a micromechanical point of view, this distribution is associated with diffusionally
 280 accommodated grain-boundary sliding for which dissipation varies monotonically with
 281 temperature and period. The creep function of the material takes the form

$$J(t) = J_U \left[1 + \Delta \int_{\tau_L}^{\tau_H} D(\tau) \left[1 - \exp \left(-\frac{t}{\tau} \right) \right] d\tau + \frac{t}{\tau_M} \right], \quad (14)$$

282 where Δ is the fractional increase in compliance associated with complete anelastic re-
 283 laxation and is called the anelastic relaxation strength. A commonly used distribution of
 284 anelastic relaxation times associated with the monotonic background dissipation is the ab-

285 sorption band model proposed by *Minster and Anderson* [1981]

$$D_B(\tau) = \frac{\alpha\tau^{\alpha-1}}{\tau_H^\alpha - \tau_L^\alpha}, \quad 0 < \alpha < 1, \quad (15)$$

286 for $\tau_L < \tau < \tau_H$ and zero elsewhere. *Jackson and Faul* [2010] found that their experi-
 287 mental data were better fit by including a dissipation peak in the distribution of anelastic
 288 relaxation times, which is superimposed upon the monotonic background along with the
 289 associated dispersion. This background peak is mostly attributed to sliding with elastic
 290 accommodation of grain-boundary incompatibilities [see *Takei et al.*, 2014, for a different
 291 view]. The distribution for such a peak is given by

$$D_P(\tau) = \frac{1}{\sigma\tau\sqrt{2\pi}} \exp\left(-\frac{\ln(\frac{\tau}{\tau_P})}{2\sigma^2}\right). \quad (16)$$

292 With this, the components of the dynamic compliance become

$$\Re[\hat{J}(\omega)] = J_U \left(1 + \Delta \int_{\tau_L}^{\tau_H} \frac{D(\tau)}{1 + \omega^2\tau^2} d\tau\right), \quad (17)$$

$$\Im[\hat{J}(\omega)] = J_U \left(\omega\Delta \int_{\tau_L}^{\tau_H} \frac{\tau D(\tau)}{1 + \omega^2\tau^2} d\tau + \frac{1}{\omega\tau_M}\right). \quad (18)$$

294 Note that τ_L and τ_H define the cut-offs of the absorption band, where dissipation is frequency-
 295 dependent ($\propto \omega^\alpha$). The lower bound of the absorption band ensures a finite shear modulus
 296 at high frequencies and restricts attenuation at these periods.

297 All involved timescales (τ_M , τ_L , τ_H , and τ_P) are considered to be grain size-, pressure-
 298 , and temperature-dependent through [*Jackson and Faul*, 2010]

$$\tau_i(T, P, d) = \tau_{i0} \left(\frac{d_g}{d_0}\right)^{m_g} \exp\left[\left(\frac{E^*}{R}\right)\left(\frac{1}{T} - \frac{1}{T_0}\right)\right] \exp\left[\left(\frac{V^*}{R}\right)\left(\frac{P}{T} - \frac{P_0}{T_0}\right)\right], \quad (19)$$

299 where all parameters are as before (cf. Eq 12) and $i = M, L, H, P$. The grain size exponent
 300 m_g can be different in the case of anelastic (m_{ga} for $i = L, H, P$) and viscous relaxation
 301 (m_{gv} for $i = M$), respectively. To more realistically account for variations of the unre-
 302 relaxed shear modulus with temperature and pressure, *Jackson and Faul* [2010] suggest the
 303 following modification

$$J_U(T, P) = \left[G_U(T_0, P_0) + (T - T_0)\frac{\partial G_U}{\partial T} + (P - P_0)\frac{\partial G_U}{\partial P}\right]^{-1}. \quad (20)$$

304 Values for the temperature and pressure derivatives are given in Table A.1.

305 2.2.3 Andrade

306 Whereas the extended Burgers model incorporates a distribution of relaxation times
 307 within a restricted time-scale to account for the transient anelastic relaxation, Andrade's

308 model proposes a distribution of relaxation times in the entire time domain (represented
 309 by arrows on spring and dashpot). The resultant configuration of a Maxwell module and a
 310 “modified” Voigt module (E4) is illustrated in Figure 2, which results in a creep function
 311 of the form [Andrade, 1962]

$$J(t) = \underbrace{J_U}_{E1} + \underbrace{\beta t^\alpha}_{E4} + \underbrace{\frac{t}{\eta}}_{E2}, \quad (21)$$

312 where β qualitatively has the same role as Δ in the extended Burgers model, and α repre-
 313 sents the frequency-dependence of the compliance. In this model, the absorption band ex-
 314 tends from 0 to ∞ . This implies that anelastic relaxation effectively contributes across the
 315 entire frequency range from short-period seismic waves to geological time-scales. Conse-
 316 quently, Andrade’s model is more economically parameterized than the extended Burgers
 317 model. Real and imaginary parts of the dynamic compliance are

$$\Re[\hat{J}(\omega)] = J_U \left[1 + \beta^* \Gamma(1 + \alpha) \omega^{-\alpha} \cos\left(\frac{\alpha\pi}{2}\right) \right], \quad (22)$$

$$\Im[\hat{J}(\omega)] = J_U \left[\beta^* \Gamma(1 + \alpha) \omega^{-\alpha} \sin\left(\frac{\alpha\pi}{2}\right) + \frac{1}{\omega\tau_M} \right], \quad (23)$$

318 where $\beta^* = \beta/J_U$ and Γ is the Gamma function. Note that Andrade’s model incorporates
 319 a broader absorption band (theoretically of infinite width) compared to the extended Burg-
 320 ers model, which ultimately results in frequency-dependent dissipation at all time-scales.
 321 Following *Jackson and Faul* [2010], corrections due to grain size, temperature, and pres-
 322 sure are applied through a pseudo-period master variable, X , which replaces the actual
 323 period
 324

$$X = \omega^{-1} \left(\frac{d_g}{d_0} \right)^{-m_g} \exp \left[\left(\frac{-E^*}{R} \right) \left(\frac{1}{T} - \frac{1}{T_0} \right) \right] \exp \left[\left(\frac{-V^*}{R} \right) \left(\frac{P}{T} - \frac{P_0}{T_0} \right) \right]. \quad (24)$$

325 **2.2.4 Sundberg-Cooper**

326 To model dissipation for the combined effects of diffusional background and elastically-
 327 accommodated grain-boundary sliding, *Sundberg and Cooper* [2010] introduce a compos-
 328 ite creep function. Their model represents a modification to Andrade’s model in order to
 329 improve its functionality over a broader frequency range and to account for the variation
 330 of the “felt” elastic response as it has to match the unrelaxed compliance (J_U) at high fre-
 331 quencies and the relaxed compliance (J_R) at low frequencies. This model graphically con-
 332 sists of two Voigt modules and a Maxwell module (cf. Figure 2); One module is similar
 333 to that used in Andrade’s model (E4), whereas the other module is equivalent to that of

334 the extended Burgers model (E3). The creep function for the Sundberg-Cooper model is
 335 thus

$$J(t) = \underbrace{J_U}_{\text{E1}} + \underbrace{\delta J \left[1 - \exp\left(-\frac{t}{\tau}\right) \right]}_{\text{E3}} + \underbrace{\beta t^\alpha}_{\text{E4}} + \underbrace{\frac{t}{\eta}}_{\text{E2}}, \quad (25)$$

336 where all variables are as before. Similar to what has been implemented in the extended
 337 Burgers model, the corresponding term (E3 in Eq. 25), can be replaced by an integral
 338 specifying a distribution of anelastic relaxation times τ as prescribed by Eq. 14 and mod-
 339 ifications for grain size, temperature, and pressure are allowed for through equation 19.
 340 Also, accounting for the influence of these parameters in the “modified” Voigt module (E4
 341 in Eq. 25) is implemented in a similar fashion to Andrade’s model through the pseudo-
 342 period master variable X (Eq. 24). With this in mind, the real and imaginary parts of the
 343 dynamic compliance for Sundberg-Cooper’s model are:

$$\Re[\hat{J}(\omega)] = J_U \left[1 + \beta^* \Gamma(1 + \alpha) \omega^{-\alpha} \cos\left(\frac{\alpha\pi}{2}\right) + \Delta \int_{\tau_L}^{\tau_H} \frac{D(\tau)}{1 + \omega^2 \tau^2} d\tau \right], \quad (26)$$

$$\Im[\hat{J}(\omega)] = J_U \left[\beta^* \Gamma(1 + \alpha) \omega^{-\alpha} \sin\left(\frac{\alpha\pi}{2}\right) + \omega \Delta \int_{\tau_L}^{\tau_H} \frac{\tau D(\tau)}{1 + \omega^2 \tau^2} d\tau + \frac{1}{\omega \tau_M} \right]. \quad (27)$$

345 2.2.5 Power-law Approximation

346 As a final model, we consider a power-law approximation, which was originally pro-
 347 posed as a means of fitting earlier measurements [Jackson *et al.*, 2002]. This model is not
 348 based on physical principles, but merely represents an approximation of shear dissipation.
 349 This power-law scheme requires that $Q_\mu^{-1} \ll 1$. Similar to the Andrade and Sundberg-
 350 Cooper models, this model also employs a pseudo-period master variable to account for
 351 the effects of temperature, pressure, and grain size, defined similar to X in Eq. 24 with m_g
 352 = 1 [Jackson and Faul, 2010]. The power-law for Q_μ takes the form

$$Q_\mu^{-1} = AX^\alpha, \quad (28)$$

353 where A is the power-law coefficient. The shear modulus dispersion associated with this
 354 dissipation model is

$$\frac{G(\omega)}{G_U} = 1 - \cot\left(\frac{\alpha\pi}{2}\right) Q_\mu^{-1}(\omega). \quad (29)$$

355 2.3 Comparing the sensitivity of the rheological models

356 Before applying the aforementioned dissipation models to Mars, it would be infor-
 357 mative to consider the sensitivity of intrinsic material properties to a number of key vari-

ables. Here, we focus on the dispersion of shear modulus G_R and attenuation factor Q_μ with forcing period, temperature, and grain size (all at constant pressure), which is shown in Figure 3. All parameter values used to compute the response curves are compiled in Table A.1. First off, we notice that both G_R and Q_μ vary considerably within the range of forcing periods considered here, which includes the tidal forcing periods of the Sun and Phobos and those of long- and short-period seismic waves (vertical lines on Figure 3a and Figure 3b). Most of the short-period seismic band (periods <1 hr) is governed by a broad, low-relaxation strength, high-frequency plateau (arrow in Figure 3b), characteristic of elastically-accommodated grain-boundary sliding (E3 in Figure 2), which for tidal periods (>1 hr) gives way to a continuous distribution of anelastic relaxation times characteristic of the high-temperature background (E4 in Figure 2). It has to be noted though that the exact location (in time) of the various processes is currently not well resolved. In general, the same features are observed in the plots showing temperature variations (Figure 3, plots c and d) in most of the ranges of interest for tidal studies. In the range of high Q_μ , i.e., short periods, low temperatures, and large grain sizes, the behaviour of the extended Burgers and Sundberg-Cooper models is due to the existence of a background dissipation peak (less apparent) associated with elastically-accommodated grain-boundary sliding (E3), which occurs around 1300–1400 K, although the interpretation of the background peak is less clear and is currently unexplained by any existing model [Takei *et al.*, 2014; Raj and Ashby, 1975; Gribb and Cooper, 1998]. Based on the relative variation of the response curves, we would expect to see little difference between the Andrade, extended Burgers, and Sundberg-Cooper models. Seismically, i.e., in terms of the relaxed shear modulus behaviour, Andrade and the extended Burgers models are similar as expected based on Figure 2, while the response of the Sundberg-Cooper model is expected to be slightly different in the seismic band.

Relative to forcing period and temperature, Q_μ appears to vary little with grain size (Figure 3, plot e), whereas G_R undergoes significant changes for very small grain sizes (<0.1 mm) (Figure 3, plot f). In contrast, the largest changes in Q_μ occur in the range of relatively large grain sizes (10–100 mm) and, because of the relative flatness of the extended Burgers and Sundberg-Cooper models in this range, compared to Andrade and power-law, respectively, the latter two are more likely to resolve (large) grain sizes. Also, since small grain sizes are accompanied by a considerable reduction in G_R , which is equivalent to an overall “softening”, and, as a consequence, a potentially significant

391 change in tidal response, small grain sizes are less likely to accord with observations. In-
 392 cidentally, the grain-size insensitivity of the extended Burgers model, in addition to pref-
 393 erential sampling of relative large grain sizes, was observed in our previous work [*Khan*
 394 *et al.*, 2018].

395 It is readily recognized from this comparison that the behaviour of Maxwell’s model
 396 is distinct. In fact, the aforementioned lack of a transient response from elastic to viscous
 397 behaviour is clearly visible in Figure 3 as a sudden drop-off in G_R . While the Maxwell
 398 model clearly shows evidence of frequency-dependent dissipation, the latter is too strong
 399 to be representative of dissipation in planetary materials. As indicated in Figure 3, the
 400 tidal periods of Mars lie in the intermediate range, where a composite of both elastic and
 401 viscous regimes contribute to the response – a feature that is incompatible with Maxwell’s
 402 model. This will be discussed further in section 5.2.4. As for the power-law, the other
 403 simplified rheological model, it shows behaviour that appears compatible with the three
 404 main models in the restricted range of low temperatures, seismic periods (~ 1 s–30 min),
 405 and larger grain sizes. However, since this model, like Andrade, lacks a cut-off in the
 406 frequency-dependent absorption band, both show similar behaviour in the aforementioned
 407 parameter range.

408 As a preliminary summary, we can make the following predictions: 1) the response
 409 of Maxwell’s model is such that it is unlikely to match geophysical observations through-
 410 out most of the period range of interest; 2) the long-period and high-temperature behaviour
 411 of the power-law scheme is not realistic; 3) the Andrade, extended Burgers, and Sundberg-
 412 Cooper models provide qualitatively similar responses over most of the period and temper-
 413 ature range considered here, although Andrade, as expected, is less dissipative at the very
 414 longest periods and highest temperatures. The similarity of the three models is not unsur-
 415 prising given that they contain many of the same elements as shown in Figure 2. These
 416 observation will be quantitatively assessed in the following, where the laboratory-based
 417 dissipation models are combined with geophysical inverse modeling.

427 **3 Geophysical data**

430 In this study we focus on mean density ($\bar{\rho}$), normalized mean moment of inertia
 431 (I/MR^2), and tidal response in the form of the second-degree tidal Love number (k_2) and
 432 global tidal dissipation or tidal quality factor (Q_2). The data are discussed in detail in the
 433 literature [e.g., *Yoder et al.*, 2003; *Lainey et al.*, 2007; *Konopliv et al.*, 2016; *Genova et al.*,

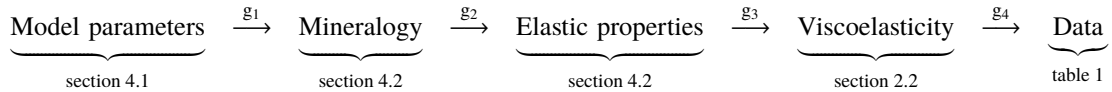
| Quantity | Symbol | Value and Uncertainty | Reference |
|------------------------|--------------|--|---------------------------------|
| Mean density | $\bar{\rho}$ | $3935 \pm 1.2 \text{ kg/m}^3$ | <i>Rivoldini et al.</i> [2011] |
| Mean moment of inertia | I/MR^2 | 0.36379 ± 0.0001 | <i>Konopliv et al.</i> [2016] |
| Tidal Love number | k_2 | 0.169 ± 0.006 | <i>Konopliv et al.</i> [2016] |
| Global quality factor | Q_2 | 95 ± 10 | <i>Khan et al.</i> [2018] |
| Mass | M | $6.417 \cdot 10^{23} \pm 2.981 \cdot 10^{19} \text{ kg}$ | <i>Konopliv et al.</i> [2016] |
| Radius | R | 3389.5 km | <i>Seidelmann et al.</i> [2002] |

428 **Table 1.** Martian geophysical data, uncertainties, and sources. Tidal Love number and global quality factor
429 are referenced to the main tidal period of Phobos (5.55 hr).

434 2016; *Rivoldini et al.*, 2011; *Nimmo and Faul*, 2013; *Khan et al.*, 2018] and need not be
435 repeated here. The geophysical data are summarized in Table 1.

436 **4 Computational aspects**

437 Formally, predicting data (**d**) from a set model parameters (**m**) is usually written as
438 $\mathbf{d} = \mathbf{g}(\mathbf{m})$, where **g** embodies the physical laws that connect **m** and **d**. In the present case,
439 **g** comprises a set of algorithms (g_1, \dots, g_4) as a result of which $\mathbf{d} = \mathbf{g}(\mathbf{m})$ can be written
440 as



441 In the following, we describe the steps needed to compute “synthetic” data ($\bar{\rho}$, I/MR^2 , k_2 ,
442 and Q_2) from the model parameters.

443 **4.1 Model parameterisation and prior model distribution**

444 We assume a spherically symmetric model of Mars consisting of crust, lithosphere,
445 mantle, and core as illustrated in Figure 4.

446 *Crust and mantle.* In line with our previous work [*Khan and Connolly*, 2008; *Khan*
447 *et al.*, 2018], crust and mantle compositions are parameterized in terms of major element
448 composition in the model chemical system CFMASNa (comprising the oxides of the ele-
449 ments CaO-FeO-MgO-Al₂O₃-SiO₂-Na₂O); a system that accounts for more than 98% of
450 the mass of Mars’ silicate envelope. Crust and mantle compositions are fixed in this study

451 and are compiled in Table 3. The crust is further parameterized in terms of thickness and
 452 surface porosity. Porosity γ is assumed to vary linearly from the surface to the bottom
 453 of the Moho (of thickness d_{crust}), where porosity vanishes due to pressure. The litho-
 454 sphere is described by thickness (d_{lit}) and temperature (T_{lit}). Within the crust and litho-
 455 sphere, temperature is computed by a linear areothermal gradient that is determined from
 456 a fixed surface temperature ($T_{surface}$) and lithospheric temperature and depth. The sub-
 457 lithospheric mantle adiabat is defined by the entropy of the lithology at the temperature
 458 T_{lit} and at depth d_{lit} , which also defines the location where the conductive lithospheric
 459 geotherm intersects the mantle adiabat. *Mantle viscoelasticity*. Parameters needed to com-
 460 pute mantle viscoelasticity depend on the chosen rheological model (section 2.2). The two
 461 important parameters that are common to all of the rheological models are grain size (d_g)
 462 and frequency-dependence (α). In addition to these two parameters, we consider anelas-
 463 tic relaxation strengths Δ_B and β and Andrade-model coefficient A as variable parameters
 464 given their importance in determining viscoelastic behaviour. Activation energy (E^*) and
 465 volume (V^*) were shown to be of less relevance in our previous work [Khan *et al.*, 2018].
 466 All other viscoelastically-related parameters are fixed and given in Table A.1.

467 *Core*. As in most geophysical models of Mars, we assume that S is the dominant
 468 light element 1) because Si, C, and O are not sufficiently soluble in an Fe-rich liquid
 469 at the low pressures that are expected to have been maintained during core formation
 470 [Stevenson, 2001] and 2) because of the observed depletion of chalcophile elements, no-
 471 tably S, of the Martian meteorites [McSween and McLennan, 2014]. Following previous
 472 work [e.g., Rivoldini *et al.*, 2011; Khan *et al.*, 2018], the core is assumed to be liquid, con-
 473 vecting, and well-mixed, and parameterised in terms of radius (r_{core}), Sulphur content
 474 (X_S), and temperature (adiabat). The core adiabat is not independent of the mantle adi-
 475 abat, but determined so that the thermodynamically-computed temperature at the core-
 476 mantle-boundary provides the input temperature for the core adiabat.

480 Finally, all parameters and prior model parameter distributions are summarised in
 481 tables 2–4.

486 4.2 Computing elastic and viscoelastic properties

487 To compute stable mantle mineralogy, seismic wave velocities, and density along
 488 self-consistent mantle adiabats as functions of pressure and composition in the CFMASNa
 489 model chemical system, we follow previous work [e.g., Khan and Connolly, 2008; Khan

| Viscoelastic model | Parameters and prior information | | | | |
|--------------------|----------------------------------|-------------|------------------------|------------|------------|
| | α | d_g (mm) | β | Δ_B | A |
| Distribution | Uniform | Log-uniform | Log-uniform | Uniform | Uniform |
| Andrade | 0.2–0.6 | 0.001–50 | 10^{-14} - 10^{-9} | – | – |
| Extended Burgers | 0.2–0.6 | 0.001–50 | – | 0.9–2 | – |
| Power-law | 0.2–0.6 | 0.001–50 | – | – | 0.001–0.01 |
| Sundberg-Cooper | 0.2–0.6 | 0.001–50 | 10^{-14} - 10^{-9} | 0.9–2 | – |

482

Table 2. Viscoelastic model parameters and prior distributions.

| Component | Crust | Mantle |
|--------------------------------|-------|--------|
| CaO | 7.0 | 2.4 |
| FeO | 18.8 | 18.7 |
| MgO | 9.2 | 30.7 |
| Al ₂ O ₃ | 10.9 | 3.5 |
| SiO ₂ | 50.7 | 44.1 |
| Na ₂ O | 3.3 | 0.6 |

483

Table 3. Major element crust and mantle compositions used in this study. Crust and mantle compositions

484

are from *Taylor and McLennan* [2008] and *Taylor* [2013]. All numbers in weight percent.

| Parameter | Description | Interval | Distribution |
|---------------|--|-------------|--------------|
| γ | Surface porosity | 0.5–0.65 | Uniform |
| d_{crust} | Crustal thickness | 10–90 km | Uniform |
| Q_{lit} | Shear attenuation in crust and lithosphere | 1000 | fixed |
| $T_{surface}$ | Surface temperature | 0 °C | fixed |
| d_{lit} | Lithospheric depth | 100–400 km | Uniform |
| T_{lit} | Lithospheric temperature | 700–1450 °C | Uniform |
| r_{core} | Core radius | 0–3000 km | Uniform |
| X_S | Core sulfur content | 0–100 % | Uniform |

485

Table 4. Crust, lithosphere, mantle, and core model parameters and prior distributions.

490 *et al.*, 2018] and employ Gibbs free energy minimization [Connolly, 2009]. For this pur-
 491 pose, the thermodynamic formulation of *Stixrude and Lithgow-Bertelloni* [2005b] and pa-
 492 rameters of *Stixrude and Lithgow-Bertelloni* [2011] are used. Pressure is obtained by in-
 493 tegrating the surface load. In the context of computing mantle properties, we would like
 494 to note that the pressure and temperature derivatives of the shear modulus (Eq. 20) em-
 495 ployed earlier (section 2.3), are not used here as these are determined as part of the free
 496 energy minimization. To account for the effect of porosity on crustal seismic P- and S-
 497 wave velocities (V_P and V_S) and density (ρ), all three parameters are multiplied by the
 498 depth-dependent porosity.

499 To compute elastic properties of the core in the FeS system, we rely on the parame-
 500 terisation of *Rivoldini et al.* [2011] as also implemented in our previous work [*Khan et al.*,
 501 2018]. Arguments for S as the main light alloying element in Mars’s core are summarised
 502 in [e.g., *Rivoldini et al.*, 2011; *Khan et al.*, 2018; *Smrekar et al.*, 2019]. The core is as-
 503 sumed to be homogeneous, fully convecting, and completely molten [e.g., *Lognonné and*
 504 *Mosser*, 1993; *Zharkov and Gudkova*, 1997; *Yoder et al.*, 2003]. Since the core is assumed
 505 to be fluid, it does not support shear and consequently no shear dissipation occurs. Hence,
 506 its response only includes the buoyant component and it is completely in quadrature with
 507 the acting force. In line with previous work, bulk dissipation is considered negligible. Fi-
 508 nally, to “convert” the elastic (unrelaxed) shear moduli to viscoelastic (relaxed) moduli, we
 509 compute shear attenuation (Q_μ) and relaxed shear moduli using the equations described
 510 in section 2.2 for each of the rheological models. Shear attenuation in the crust and litho-
 511 sphere is fixed to $Q_{lit} = 1000$. As for the core, we assume that dissipation only occurs in
 512 shear. This seems appropriate given that dissipation in bulk is negligible [*Benjamin et al.*,
 513 2006].

514 **4.3 Computing tidal response**

515 To determine the frequency-dependent tidal response of a spherically symmetric,
 516 self-gravitating, and viscoelastic planetary model, we use an adaptation of the method and
 517 code developed by *Al-Attar and Tromp* [2014] and *Crawford et al.* [2018] for modeling
 518 glacial loading. This approach is based on the generalised spherical harmonic expansions
 519 (Phinney & Burridge 1973) of the displacement field and gravitational potential pertur-
 520 bation, and leads to a complete decoupling between the radial expansions coefficients for
 521 each spherical harmonic degree and order. The resulting ordinary differential equations

522 are then efficiently solved using a one-dimensional spectral element discretisation. Inertial
 523 terms in the equations of motion are neglected within these calculations due to the tidal
 524 periods being well below those of the gravest free oscillations. Quasi-static deformation in
 525 the fluid core is modelled following the approach of *Dahlen* [1974], with the inclusion of
 526 tidal forces requiring a slight modification of the theory as described in appendix B. The
 527 resulting code can calculate the Love numbers k_n , h_n , and l_n along with the quality fac-
 528 tors Q_n for any spherical harmonic degree. Mean density and mean moment of inertia are
 529 readily obtained from integration of the density profile.

530 4.4 Inverse problem

531 Following our previous work, the inverse problem $\mathbf{d} = \mathbf{g}(\mathbf{m})$ is solved using a Bayesian
 532 approach [e.g., *Mosegaard and Tarantola*, 1995]

$$\sigma(\mathbf{m}) = \kappa f(\mathbf{m})\mathcal{L}(\mathbf{m}), \quad (30)$$

533 where κ is a normalization constant, $f(\mathbf{m})$ is the prior model parameter distribution, $\mathcal{L}(\mathbf{m})$
 534 is the likelihood function, and $\sigma(\mathbf{m})$ is the posterior model parameter distribution and rep-
 535 represents the solution to the inverse problem. The form of $\mathcal{L}(\mathbf{m})$ is determined from data,
 536 their uncertainties, and data noise modelling (to be described below). To sample the poste-
 537 rior distribution, we employ the Metropolis algorithm, which is an importance sampling
 538 algorithm. This stochastic algorithm, which is based on a Markov chain Monte Carlo
 539 method, ensures that models that fit data (through $\mathcal{L}(\mathbf{m})$) and are consistent with the cho-
 540 sen prior model parameter distribution (through $f(\mathbf{m})$) are sampled preferentially.

541 As concerns the likelihood function, we assume that data noise is Gaussian dis-
 542 tributed and that observational uncertainties and modeling errors among the different data
 543 sets are independent. As a consequence, the likelihood function takes the form

$$\mathcal{L}(\mathbf{m}) \propto \prod_i \exp\left(-\frac{|\mathbf{d}_{\text{obs}}^i - \mathbf{d}_{\text{cal}}^i(\mathbf{m})|^2}{2\sigma_i^2}\right), \quad (31)$$

544 where the integer i is either $\bar{\rho}$, I/MR^2 , k_2 , or Q_2 , and \mathbf{d}_{obs} and $\mathbf{d}_{\text{cal}}(\mathbf{m})$ refer to observed
 545 and calculated ‘‘synthetic’’ data, respectively, and σ is the uncertainty associated with each
 546 data set. For each rheological model, we sampled around 100,000 models in total and to
 547 ensure near-independence, every 20th model was retained for analysis. This number is
 548 obtained from analysing the autocorrelation of the likelihood function, which provides a
 549 measure of when independence between models has been achieved.

5 Results and discussion

5.1 Data Fit

Here and in the following, the main focus will be on the power-law approximation scheme, and the extended Burgers, Andrade, and Sundberg-Cooper rheological models; Maxwell's model will be discussed separately in section 5.2.4. We make this distinction here based on the observation that although Maxwell's model is capable of fitting the observations (not shown), this is only achievable for unrealistically low mean viscosities ($\sim 10^{16}$ Pa-s, see section 5.2.4). The resultant data fits are shown in Figure 5 and indicate that all four rheological models are capable of fitting the observations within uncertainties.

5.2 Viscoelastic properties

5.2.1 Grain size

The sampled grain-size distributions for each of the rheological models is shown in Figure 6 and indicate that the Andrade, Sundberg-Cooper, and power-law models imply larger grain sizes in comparison to the predictions based on the extended Burgers model. The three former models suggest most probable grain sizes in the range 0.5–4 cm range, whereas in the case of the latter model, grain sizes are less well-resolved with a slight preference in the range 0.1–1 cm. Importantly, the form of the sampled grain size distributions follows the behaviour observed in Figure 3 closely: Andrade, Sundberg-Cooper, and power-law models show the largest variation in the range ~ 1 –10 cm, while the extended Burgers model is relatively “flat” in the 0.1–10 cm range, in agreement with our earlier work [Khan *et al.*, 2018].

In general, grain sizes obtained in this study are larger than observed in terrestrial samples, where grains of submillimeter-to-millimeter size are typically found [Karato, 1984]. Incidentally, relatively large grain sizes (~ 1 –10 cm) are also found in a study by Lau and Faul [2019], where the extended Burgers model was applied to Earth's deep mantle to model its anelastic response (see also section 5.2.2).

In support of larger grain sizes, we showed in our previous work [Khan *et al.*, 2018] how the geophysical results could be employed in tandem with geodynamic simulations to identify plausible geodynamic scenarios and parameters. The geodynamical models were generally able to reproduce the geophysically-determined areotherms, crustal thickness values, and grain sizes, but, in part only, lithospheric thicknesses. Grain sizes greater than

| Parameter | Andrade | Extended Burgers | Power-law | Sundberg-Cooper |
|---------------------|-----------|------------------|---------------|-----------------|
| d_g | 0.1–2 cm | 0.01–4 cm | 0.1–2 cm | 1–4 cm |
| α | 0.22–0.38 | 0.22–0.42 | 0.22–0.38 | 0.24–0.38 |
| $-\log_{10}(\beta)$ | 12.4–13 | – | – | 13.5–14 |
| Δ_B | – | 1–1.5 | – | 1.1–1.4 |
| A | – | – | 0.0015–0.0025 | – |

593 **Table 5.** Summary of inversion results for the viscoelastic model parameters considered in this study.

594 Quoted ranges cover the 90% credible interval.

586 1 mm were mainly restricted to cases of relatively strong grain growth, which tended to
 587 increase internal temperature and thicken the lithosphere beyond the current geophysical
 588 observations.

590 For brevity, inversion results for the other viscoelastic model parameters considered
 591 here, including frequency exponent (α), anelastic relaxation strengths (Δ_B and β), and
 592 power-law coefficient (A), are summarised in Table 5.

595 **5.2.2 Temperature and attenuation**

596 Inverted areothermal and shear attenuation (Q_μ) profiles are shown in Figure 7 for
 597 the major rheological models considered in this study. From this figure, we can make a
 598 number of observations. Firstly, the obtained thermal profiles are well-constrained and
 599 overlap across the entire depth range. This confirms earlier investigations [*Nimmo and*
 600 *Faul, 2013; Khan et al., 2018*], where it was shown that global tidal dissipation provides
 601 strong constraints on thermal structure. Moreover, the temperature profiles are in good
 602 agreement with the results for the extended Burgers model of *Khan et al.* [2018]. Also,
 603 this suggests that the obtained temperature profiles are to first order independent of rhe-
 604 ology. Secondly, the shear attenuation profiles overlap in the upper mantle (depth range
 605 200–1000 km), which appears to be highly attenuating with $Q_\mu < 100$, but differ in the
 606 lower part of the mantle (depth range 1000–1600 km), where Q_μ appears to be less con-
 607 strained for the Andrade and extended Burgers models. Note that although the shear at-
 608 tenuation profiles shown in Figure 7 are computed at the main tidal period of Phobos
 609 (5.55 hr), shear attenuation at seismic periods (1 s) are not significantly different with Q_μ

610 remaining below 100 for most of the upper part of the mantle (not shown). This suggests
 611 that it will be difficult to distinguish between the various rheological models based on the
 612 structure of the attenuation profiles. From the point of view of seismology, The implica-
 613 tions of this for the propagation and observation of e.g., seismic body and surface waves
 614 is such that their detection could be significantly impaired over regional and teleseismic
 615 distances. The detection of seismic events by the InSight seismometer [Lognonné, 2019]
 616 would therefore present a first-order test of the experimentally-constrained viscoelastic
 617 models considered here in the sense that seismic waves that have spent a significant part
 618 of their traverse in the mantle from source to station are expected to be attenuated.

619 ***5.2.3 Predicted short- and long-period planetary response***

620 What the previous discussion suggests is that from knowledge of dissipation at a
 621 single frequency (here the main tidal period of Phobos), it appears to be difficult to dis-
 622 tinguish between rheological models. If, however, we know the tidal response at other
 623 frequencies, more precise arguments can be made about both interior dissipative proper-
 624 ties and corresponding rheological models as illustrated in Figure 8 [see also Lognonné
 625 *et al.*, 1996; Van Hoolst *et al.*, 2003; Zharkov and Gudkova, 2005; Smrekar *et al.*, 2019].
 626 Figure 8 shows the predicted probability distributions for k_2 and Q_2 at three different peri-
 627 ods: short- (1 s) and long-period (1 hr) seismic waves, and at the main Solar tide on Mars
 628 (12.32 hr) computed for all the inverted models. First off, relative differences in computed
 629 k_2 distributions for the three different periods for a particular rheological model are mi-
 630 nor and cover a similar range ~ 0.16 – 0.18 across all rheological models. In the case of
 631 Q_2 , however, the distinction within and between models is significantly more pronounced.
 632 Although all four rheological models match the only existing observation of Q_2 at 5.55
 633 hours (Figure 5), they differ in their prediction for Q_2 at the other periods. In particular,
 634 similar behaviour for the Andrade and power-law models, on the one hand, and the ex-
 635 tended Burgers and Sundberg-Cooper models, on the other hand, is observed. This “pair-
 636 ing” clearly reflects the common underlying mechanisms that exists between the models.
 637 For example, higher dissipation (lower Q_2) at higher frequencies observed for the former
 638 two models (Figure 8c–d and g–h) is attributed to the presence of the extra dissipation
 639 peak, which tends to flatten the Q_μ curves and, as a result, prevents a dramatic increase
 640 of attenuation at short time-scales. In contrast, since the frequency-dependent absorption
 641 band extends throughout the entire spectrum in the case of Andrade and the power-law

642 scheme, low attenuation (high Q_2) at high frequencies ensues (Figure 8a–b and e–f). Note
 643 that, although intrinsic attenuation (Q_μ) plays a key role in determining the tidal quality
 644 factor (Q_2), they are not the same. As emphasised, the discrepancy is due to the role of
 645 the restoring force of gravity, which increases in importance with increasing forcing pe-
 646 riod, but is less relevant in the case of seismic waves. Clearly, observations of dissipation
 647 at other periods, hold the potential of strongly constraining the anelastic structure.

648 This is further quantified in Figure 9, which shows the degree-two global response
 649 of Mars in the form of k_2 , Q_2 , and δ_2 over a much larger period range (~ 1 s–10 yr) for
 650 a single inverted model (maximum likelihood model for each rheology). The Q_2 response
 651 behaviour (Figure 9b) for the Andrade and power-law models appears to be dominated by
 652 the absorption band with a negative period-dependence, which, in the case of Andrade,
 653 slowly transitions into viscous dissipation for periods >1 month up until a peak value is
 654 reached (not shown) after which friction occurs purely viscously [see also discussion in
 655 *Efroimsky, 2012a*]. As expected, the power-law scheme fails to propose realistic values
 656 of Q_2 at long periods (Figure 9b), which indicates that the Chandler wobble analysis by
 657 *Zharkov and Gudkova [2009]* (with a period of ~ 200 days) that relies on this particular
 658 rheological model needs to be reassessed.

659 In comparison, the response of the extended Burgers and Sundberg-Cooper models
 660 is more complex with a broad plateau extending from the seismic into the tidal range that
 661 merges into the absorption band with negative frequency dependence (note that the slopes
 662 determined by α , i.e., the frequency exponent, between the red and black lines are differ-
 663 ent because the inverted values for α differ for the two models). On the smaller-period
 664 side of the plateau, dissipation varies with a positive frequency-dependence, whereas to-
 665 ward the long-period end of the response curves (>2 yr), purely viscous dissipation pre-
 666 dominates. For the particular models shown here, Phobos' tide falls in the absorption
 667 band in the case of the extended Burgers model, but appears within transition the plateau
 668 and the absorption band in the Sundberg-Cooper model. It has to be emphasised though
 669 that the relative location of the various features that dominate dissipation at different time-
 670 scales (see section 2.1) are not well-constrained from the observation at a single period.
 671 In summary, this figure serves to indicate that the predicted response behaviour is such
 672 that from comparison of a single measurement by InSight of Q_2 above or below and/or k_2
 673 below the main tidal period of Phobos, strong constraints on interior structure and dissipa-
 674 tive properties can be obtained.

675 This has been discussed in terrestrial and lunar studies, where data at different pe-
 676 riods are available [e.g., *Benjamin et al.*, 2006; *Nimmo et al.*, 2012; *Efroimsky*, 2012a;
 677 *Karato*, 2013; *Williams and Boggs*, 2015; *Lau and Faul*, 2019]. For example, *Lau and Faul*
 678 [2019] considered seismic normal mode and short- and long-period tidal dissipation mea-
 679 surements for the Earth in an attempt to reconcile the anelastic response of the deep man-
 680 tle across timescales from ~ 500 s to 18.6 yr. As briefly indicated earlier, the authors use
 681 the extended Burgers model and vary a number of parameters related hereto (e.g., grain
 682 size, anelastic relaxation strengths, activation energy and volume, and mantle potential
 683 temperature). The authors find that two different frequency dependencies are needed to
 684 fit normal mode and tide data. Qualitatively, the authors observe the same anelastic be-
 685 haviour discussed in relation to the extended Burgers model investigated here (red line in
 686 Figure 9), including the presence of a plateau that determines dissipation for periods be-
 687 low ~ 12 hr and an absorption band above, extending to ~ 20 yr without clear indication
 688 of onset of viscous dissipation. As is the case for our models, the exact occurrence of the
 689 various characteristics (e.g., plateau, transition to absorption band, and α) is less well-
 690 constrained.

691 Finally, we have made model predictions by computing responses at four periods
 692 (1 s, 1 hr, 5.55 hr, and 12.32 hr) for all Love numbers (k_n , h_n , and l_n), gravimetric factors
 693 δ_n , and quality factors Q_n , for the maximum likelihood models of each rheology and for
 694 $n=2-5$. The results are compiled in Table 6. The absolute value of Q_n decreases, i.e., dis-
 695 sipation increases, as n becomes larger. This reflects an increased sensitivity to shallower
 696 structure, which implies that more of the dissipative part of the planet (mantle) is “seen”
 697 with increased spherical harmonic degree. The values obtained here are in good agree-
 698 ment with model predictions made elsewhere [e.g., *Van Hoolst et al.*, 2003; *Zharkov and*
 699 *Gudkova*, 1997, 2005, 2009]. Based on the observed variation in predicted model values
 700 (Figure 9), the phase lags Q_n are likely to be much better at discriminating between dif-
 701 ferent models than are the gravimetric factors δ_n . This important finding can be examined
 702 by the measurements of dissipation provided by both RISE and SEIS. Although beyond
 703 the scope of this study, knowledge of higher-degree harmonics are important for model-
 704 ing e.g., the orbital evolution and future demise of Phobos [*Burns*, 1978; *Efroimsky and*
 705 *Lainey*, 2007; *Black and Mittal*, 2015; *Rosenblatt et al.*, 2016].

724 **5.2.4 Maxwell's Model**

725 While Maxwell's model, in spite of its simplicity, is capable of fitting data within
 726 uncertainties (not shown in Figure 5) for interior structure models that match the results
 727 of the other models (see Table 7), this is only possible for very low average viscosities
 728 ($\sim 2 \cdot 10^{16}$ Pa·s) that are well below what is expected for the viscosity of the upper mantle
 729 of the Earth (10^{19} – 10^{22} Pa·s) [e.g., *Peltier, 1974; Forte and Mitrovica, 2001; Soldati et al.,*
 730 *2009; Cathles, 2015*] and therefore probably unrealistic.

731 Low mantle viscosities have also been obtained in previous studies [e.g., *Bills et al.,*
 732 *2005*], where Maxwell's model was applied to estimate the tidal response of Mars. For
 733 a homogeneous solid model of Mars, *Bills et al. [2005]* found an average viscosity of
 734 $\sim 10^{15}$ Pa·s. *Bills et al. [2005]* argued that the presence of a liquid core could provide a
 735 possible explanation for the low viscosity, but the modeling results based on Maxwell pre-
 736 sented here invalidate this inasmuch as a model including a fully liquid core still results in
 737 a low average viscosity. We attribute the unrealistically low viscosity values obtained from
 738 Maxwell's model to its shortcoming, particularly lack of an intermediate-stage anelastic
 739 transient response as also observed elsewhere [e.g., *Castillo-Rogez and Banerdt, 2012*]. In
 740 this context, *Castillo-Rogez and Banerdt [2012]* found that anelastic transient relaxation
 741 processes are required to properly account for Mars's high tidal dissipation. Consider-
 742 ing an Andrade rheology and a Mars model with fluid-outer and solid-inner core radii of
 743 1700 km and 1100 km, respectively, they obtained more "realistic" mantle viscosities of
 744 10^{19} – 10^{22} Pa·s depending on the assumed value for α (higher α results in lower η).

745 **5.3 Interior structure**

746 Since this study focuses on modeling and understanding the anelastic response of
 747 Mars at tidal and seismic frequencies, we only briefly summarise the results on interior
 748 structure. Inverted model parameters are presented in Table 7 and profiles of P- and S-
 749 wave speed and density are shown in Figure C.1. While the results for the viscoelastic
 750 models largely overlap, it is more difficult to use the results as a means of distinguishing
 751 between rheological models with the exception of Maxwell's model. Not unsurprisingly,
 752 the results are in good agreement with those of our previous work [*Khan et al., 2018*],
 753 where the influence of compositional parameters was considered in detail in the context of
 754 an extended Burgers viscoelastic model. Here as there, models imply relatively large cores
 755 (~ 1750 – 1850 km in radius) with a significant complement of S (~ 17 – 20 wt%). As the

756 core S content found here is close to the eutectic composition and core-mantle-boundary
 757 temperatures and pressures are in excess of 1800 K and ~19–20 GPa, respectively, a solid
 758 inner core is unlikely to be present [e.g., *Stewart et al.*, 2007; *Helfrich*, 2017]. More-
 759 over, a large core implies that the counterpart of a terrestrial bridgmanite-dominated lower
 760 mantle in Mars is unlikely to be present with potentially important implications for the
 761 dynamic evolution of Mars’s mantle [e.g., *Breuer et al.*, 1997; *van Thienen et al.*, 2006;
 762 *Ruedas et al.*, 2013]. For further discussion of interior structure, we refer the reader to
 763 previous work [e.g., *Rivoldini et al.*, 2011; *Nimmo and Faul*, 2013; *Plesa et al.*, 2016; *Khan*
 764 *et al.*, 2018; *Smrekar et al.*, 2019].

765 **6 Discussion and Conclusion**

766 In this study, we have examined the geophysical implications of a series of grain-
 767 size-, temperature- and frequency-dependent laboratory-based viscoelastic models. These
 768 models have been developed in an attempt to describe dissipative properties of planetary
 769 materials on the macroscopic scale in terms of interactions that occur on the microscopic
 770 scale, i.e., on the level of atoms and grains. The rheological models are based on defor-
 771 mation experiments of melt-free polycrystalline olivine and an olivine-pyroxene mixture,
 772 respectively, and include Maxwell, Andrade, extended Burgers, Sundberg-Cooper, and a
 773 power-law scheme.

774 We combined the viscoelastic models with phase equilibrium computations to al-
 775 low for self-consistently constructed models of seismic elastic and anelastic properties
 776 and tested the resultant models against global geophysical observations for Mars. All of
 777 the models were found to be able to match the Martian observations including tidal re-
 778 sponse (amplitude and phase) and mean mass and moment of inertia. The simplest of the
 779 investigated rheological models, that of Maxwell, whose response only consists of a purely
 780 elastic and a viscous component, only matched the observations for very low viscosities
 781 ($\sim 10^{16}$ Pa·s). This observation is in accord with previous work, where similar results were
 782 obtained. Based on the observation that the main tidal periods of most solar system ob-
 783 jects are to be found in the transient period range where Maxwell is singularly deficient,
 784 it appears reasonable to conclude that Maxwell’s model should be abandoned in favour of
 785 more realistic models such as Andrade, extended Burgers, or Sundberg-Cooper. These
 786 models represent improvements relative to Maxwell inasmuch as these models include

787 an anelastic transient regime that allows for generating significant dissipation in the main
788 tidal period range.

789 Of the other models investigated, all converged upon the same results in terms of in-
790 terior structure parameters, i.e., the results are to first order insensitive of the exact nature
791 of the attenuation mechanisms that account for dissipation of energy in planetary interi-
792 ors. While we only examined a single frequency associated with the main tide of Phobos,
793 our results show that from knowledge of the response at an additional period, significantly
794 improved constraints on interior properties can be derived. InSight observations of tidal
795 phase lags will prove particularly rewarding since these appear to be a much better means
796 of discriminating between different models than either tidal amplitudes or induced surface
797 displacements.

798 As shown here, application of our method yields a host of quantitative predictions
799 and results. In particular, the method also provides insights into future requirements of,
800 e.g., improvements in experimental data, that will be needed for modeling more complex
801 models. Chief among these are (more discussion is given in *Nimmo and Faul* [2013] and
802 *Khan et al.* [2018]): a) extending the forced torsional oscillation experiments to minerals
803 beyond olivine, including compositions that are more Fe-rich and therefore more represen-
804 tative of Martian mantle compositions; b) extending the experimental conditions to longer
805 periods; c) consideration of the effects of hydration and partial melt, which can signif-
806 icantly impact viscosity by lowering it and thereby increase dissipation [*Jackson et al.*,
807 2004; *Karato*, 2013; *Takei*, 2017; *Cline II et al.*, 2018]; and d) including grain-size varia-
808 tion with depth in view of geodynamic models that show evidence for grain growth with
809 depth [e.g., *Rozel*, 2012], which would tend to lower dissipation, requiring increased dissi-
810 pation elsewhere.

811 For community use, we computed and tabulated predicted model responses (Love
812 numbers and attenuation) at a number of distinct periods and spherical harmonic degree
813 for each of the rheological models considered here. Since the amount of energy that is be-
814 ing dissipated in planetary interiors depends on rheology, the latter effectively controls the
815 orbital evolution of binaries such as Mars and Phobos and therefore provides an improved
816 means for e.g., understanding the future demise of Phobos. Penultimately, we should note
817 that while the results of this study are based on Mars, the methodology is generally appli-
818 cable to other terrestrial planets and exoplanets.

819 Ultimately, it is the expectation that InSight, which has been operative on the sur-
 820 face of Mars since the end of November 2018, will enable separate measurements of k_2 ,
 821 Q_2 , and δ_2 (and maybe k_3 and δ_3). More specifically, and in addition to the direct mea-
 822 surement of the tidal response by RISE, different schemes have been proposed to employ
 823 the SEIS instrument to extract the tidal response from the seismic data, by having the very
 824 broad-band seismometer act as a gravimeter to measure Mars’s response to tidal forces
 825 [Pou *et al.*, 2018].

826 As a final remark, we would like to note that although we have focused on Mars, the
 827 methodology developed here is generally formulated and therefore applicable to other solar
 828 and extra-solar system bodies, where tidal constraints are available to determine interior
 829 structure and properties. In particular, we envision applying our method to the Moon for
 830 which tidal dissipation measurements at several periods are available.

831 **A: Viscoelastic parameters**

832 Table A.1 compiles the viscoelastic parameter values used throughout this study.

838 **B: Further details about tidal calculations**

839 To model tidal deformation within the planet, we make use of the quasi-static mo-
 840 mentum equation [e.g., *Dahlen*, 1974; *Tromp and Mitrovica*, 1999; *Al-Attar and Tromp*,
 841 2014]

$$-\nabla \cdot \mathbf{T} + \nabla(\rho \mathbf{u} \cdot \nabla \Phi) - \nabla \cdot (\rho \mathbf{u}) \nabla \Phi + \rho \nabla(\phi + \psi) = \mathbf{0}, \quad (\text{B.1})$$

842 where \mathbf{T} denotes the incremental Lagrangian-Cauchy stress tensor, ρ the equilibrium den-
 843 sity, \mathbf{u} the displacement vector, Φ the equilibrium gravitational potential, ϕ the perturbed
 844 gravitational potential, and ψ is the tidal potential that we have now added into the prob-
 845 lem. The sign conventions used in this section follow those in *Al-Attar and Tromp* [2014].
 846 The tidal potential is assumed to have an exponential time-dependence at a given forcing
 847 frequency. Due to the linearity of the equations of motion, the displacement and grav-
 848 itational potential have the time-dependence, and the common exponential factors have
 849 been canceled from all equations. The frequency-dependence within the problem then
 850 arises solely from the fact that the appropriate viscoelastic moduli are evaluated at the
 851 prescribed tidal frequency.

852 As shown by *Dahlen* [1974], for static or quasi-static problems this linearised La-
 853 grangian description is only valid within solid parts of the Earth model. Within the fluid

854 core, the displacement vector is not well-defined, and *Dahlen* [1974] instead showed that
 855 all relevant fields can be expressed in terms of the perturbed gravitational potential ϕ . In
 856 particular, we can write the first-order perturbations to density ρ' and pressure p' in the
 857 fluid core as

$$p' = -\rho(\phi + \psi), \quad \rho' = g^{-1} \partial_r \rho(\phi + \psi), \quad (\text{B.2})$$

858 where $g = \partial_r \Phi$. These identities generalise those presented in *Dahlen* [1974] to include
 859 the applied tidal potential, but their derivation is essentially unchanged. The gravitational
 860 potential perturbation itself is then a solution of the following modified Poisson equation

$$(4\pi G)^{-1} \nabla^2 \phi = \begin{cases} -\nabla \cdot (\rho \mathbf{u}) & \text{in solid regions} \\ g^{-1} \partial_r \rho(\phi + \psi) & \text{in fluid regions} \\ 0 & \text{outside the planet} \end{cases} \quad (\text{B.3})$$

861 where G is Newton's gravitational constant. The boundary and continuity conditions for
 862 the problem can be found in detail in *Al-Attar and Tromp* [2014]. Within the tidal prob-
 863 lem, however, there is no applied surface load, while the tidal potential ψ appears within
 864 the continuity conditions on the linearised traction across fluid-solid boundaries via its oc-
 865 currence in the pressure perturbation p' in fluid regions.

866 For numerical work, it is most convenient to express the problem in its weak form.
 867 The derivation follows closely that given in *Al-Attar and Tromp* [2014], requiring only
 868 slight changes due to the inclusion of the tidal potential in the momentum equation, the
 869 modified Poisson equation, and in the traction boundary conditions at fluid-solid bound-
 870 aries. The final result is given by

$$\begin{aligned} \mathcal{A}(\mathbf{u}, \phi | \mathbf{u}', \phi') &+ \int_{M_S} \rho \nabla \psi \cdot \mathbf{u}' \, dV + \int_{M_F} g^{-1} \partial_r \rho \psi \phi' \, dV \\ &+ \int_{\Sigma_{FS}} \rho^- \psi \mathbf{u}' \cdot \hat{\mathbf{n}} \, dS - \int_{\Sigma_{SF}} \rho^+ \psi \mathbf{u}' \cdot \hat{\mathbf{n}} \, dS = 0, \end{aligned} \quad (\text{B.4})$$

871 where \mathcal{A} is the bilinear form defined in eq.(2.52) of *Al-Attar and Tromp* [2014], (\mathbf{u}', ϕ')
 872 are test functions for the displacement and potential, respectively, M_S denotes the solid
 873 regions of the model, M_F the fluid regions, Σ_{FS} and Σ_{SF} denote the fluid-solid bound-
 874 aries, where the first subscript indicates whether the region on the inside of the boundary
 875 is solid (S) or fluid (F), and finally ρ^- and ρ^+ denote, respectively the equilibrium density
 876 evaluated on the lower or upper sides of a boundary. As the tidal potential only modifies
 877 the force term for the problem, the numerical implementation was readily made within
 878 the loading code developed by *Al-Attar and Tromp* [2014], which has been subsequently
 879 refined and improved by *Crawford et al.* [2018].

880 C: Seismic wave speed and density profiles

881 Figure C.1 shows sampled P - and S -wave speed and density profiles from the sur-
 882 face to the centre of Mars for each of the rheological models considered here. As the
 883 figures also shows, the particular choice of rheological model does not appear to make a
 884 substantial difference, since the solutions for the various viscoelastic models largely over-
 885 lap. In the context of investigating the influence of compositional variations, [Khan *et al.*,
 886 2018] examined four other bulk Martian compositions (*Sanloup et al.* [1999], *Lodders and*
 887 *Fegley* [1997], *Dreibus and Wänke* [1984], *Morgan and Anders* [1979]) that resulted in
 888 models that are consistent with the present results (see also section 5.3).

891 Acknowledgments

892 We are grateful to two anonymous reviewers for comments that improved the manuscript.
 893 We would also like to thank Michael Efroimsky and Francis Nimmo for additional sug-
 894 gestions. This work was supported by a grant from the Swiss National Science Foundation
 895 (SNF project 172508 “Mapping the internal structure of Mars”). This is InSight contribu-
 896 tion number 92. The interior structure models computed here, including inverted model
 897 parameters, are available online at: [https://github.com/bagheriamirh/Tidal-Response-of-](https://github.com/bagheriamirh/Tidal-Response-of-Mars-JGR)
 898 *Mars-JGR*.

899 References

- 900 A, G., J. Wahr, and S. Zhong (2014), The effects of laterally varying icy shell structure on
 901 the tidal response of Ganymede and Europa, *Journal of Geophysical Research (Planets)*,
 902 *119*, 659–678, doi:10.1002/2013JE004570.
- 903 Abers, G. A., K. Fischer, G. Hirth, D. Wiens, T. Plank, B. K. Holtzman, C. McCarthy, and
 904 E. Gazel (2014), Reconciling mantle attenuation-temperature relationships from seismol-
 905 ogy, petrology, and laboratory measurements, *Geochemistry, Geophysics, Geosystems*,
 906 *15*(9), 3521–3542.
- 907 Agnew, D. (2015), *Earth Tides. Treatise on Geophysics and Geodesy*, 151-178 pp., New
 908 York: Elsevier.
- 909 Al-Attar, D., and J. Tromp (2014), Sensitivity kernels for viscoelastic loading based
 910 on adjoint methods, *Geophysical Journal International*, *196*(1), 34–77, doi:
 911 10.1093/gji/ggt395.

- 912 Andrade, E. (1962), The validity of the $t^{1/3}$ law of flow of metals, *Philosophical Maga-*
913 *zine*, 7(84), 2003–2014.
- 914 Bellis, C., and B. Holtzman (2014), Sensitivity of seismic measurements to frequency-
915 dependent attenuation and upper mantle structure: An initial approach, *Journal of Geo-*
916 *physical Research: Solid Earth*, 119(7), 5497–5517, doi:10.1002/2013JB010831.
- 917 Benjamin, D., J. Wahr, R. D. Ray, G. D. Egbert, and S. D. Desai (2006), Constraints on
918 mantle anelasticity from geodetic observations, and implications for the J_2 anomaly,
919 *Geophysical Journal International*, 165, 3–16, doi:10.1111/j.1365-246X.2006.02915.x.
- 920 Bierson, C. J., and F. Nimmo (2016), A test for io’s magma ocean: Modeling tidal dis-
921 sipation with a partially molten mantle, *Journal of Geophysical Research: Planets*,
922 121(11), 2211–2224, doi:10.1002/2016JE005005.
- 923 Bills, B. G., G. A. Neumann, D. E. Smith, and M. T. Zuber (2005), Improved estimate
924 of tidal dissipation within Mars from MOLA observations of the shadow of Phobos,
925 *Journal of Geophysical Research (Planets)*, 110, E07004, doi:10.1029/2004JE002376.
- 926 Black, B. A., and T. Mittal (2015), The demise of phobos and development of a martian
927 ring system, *Nature Geoscience*, 8(12), 913.
- 928 Breuer, D., D. A. Yuen, and T. Spohn (1997), Phase transitions in the Martian mantle:
929 Implications for partially layered convection, *Earth and Planetary Science Letters*, 148,
930 457–469, doi:10.1016/S0012-821X(97)00049-6.
- 931 Burns, J. A. (1978), The dynamical evolution and origin of the martian moons, *Vistas in*
932 *Astronomy*, 22, 193–210.
- 933 Castillo-Rogez, J. C., and W. B. Banerdt (2012), Impact of Anelasticity on Mars’ Dissi-
934 pative Properties - Application to the InSight Mission, in *The Mantle of Mars: Insights*
935 *from Theory, Geophysics, High-Pressure Studies, and Meteorites*, LPI Contributions, vol.
936 1684, p. 4.
- 937 Castillo-Rogez, J. C., M. Efroimsky, and V. Lainey (2011), The tidal history of Iapetus:
938 Spin dynamics in the light of a refined dissipation model, *Journal of Geophysical Re-*
939 *search (Planets)*, 116, E09008, doi:10.1029/2010JE003664.
- 940 Cathles, L. M. (2015), *Viscosity of the Earth’s Mantle*, vol. 1362, Princeton University
941 Press.
- 942 Chawla, K. K., and M. Meyers (1999), *Mechanical behavior of materials*, Prentice Hall
943 Upper Saddle River.

- 944 Choblet, G., G. Tobie, C. Sotin, M. Běhounková, O. Čadek, F. Postberg, and O. Souček
 945 (2017), Powering prolonged hydrothermal activity inside enceladus, *Nature Astronomy*,
 946 *1*(12), 841.
- 947 Cline II, C., U. Faul, E. David, A. Berry, and I. Jackson (2018), Redox-influenced seismic
 948 properties of upper-mantle olivine, *Nature*, *555*(7696), 355.
- 949 Connolly, J. A. D. (2009), The geodynamic equation of state: What and how, *Geochem-*
 950 *istry, Geophysics, Geosystems*, *10*(10), n/a–n/a, doi:10.1029/2009GC002540, q10014.
- 951 Cooper, R. F. (2002), Seismic wave attenuation: Energy dissipation in viscoelastic crys-
 952 talline solids, *Reviews in mineralogy and geochemistry*, *51*(1), 253–290.
- 953 Correia, A. C., G. Boué, J. Laskar, and A. Rodríguez (2014), Deformation and tidal evolu-
 954 tion of close-in planets and satellites using a maxwell viscoelastic rheology, *Astronomy*
 955 *& Astrophysics*, *571*, A50.
- 956 Crawford, O., D. Al-Attar, J. Tromp, J. X. Mitrovica, J. Auermann, and H. C. P.
 957 Lau (2018), Quantifying the sensitivity of post-glacial sea level change to later-
 958 ally varying viscosity, *Geophysical Journal International*, *214*(2), 1324–1363, doi:
 959 10.1093/gji/ggy184.
- 960 Dahlen, F. A. (1974), On the Static Deformation of an Earth Model with a Fluid Core,
 961 *Geophysical Journal*, *36*, 461–485, doi:10.1111/j.1365-246X.1974.tb03649.x.
- 962 Dreibus, G., and H. Wänke (1984), Accretion of the earth and inner planets., in *Geochem-*
 963 *istry and Cosmochemistry*, pp. 3–11.
- 964 Dumoulin, C., G. Tobie, O. Verhoeven, P. Rosenblatt, and N. Rambaux (2017), Tidal con-
 965 straints on the interior of venus, *Journal of Geophysical Research: Planets*, *122*(6),
 966 1338–1352.
- 967 Efroimsky, M. (2012a), Tidal Dissipation Compared to Seismic Dissipation: In
 968 Small Bodies, Earths, and Super-Earths, *Astrophys. J.*, *746*, 150, doi:10.1088/0004-
 969 637X/746/2/150.
- 970 Efroimsky, M. (2012b), Bodily tides near spin–orbit resonances, *Celestial Mechanics and*
 971 *Dynamical Astronomy*, *112*(3), 283–330, doi:10.1007/s10569-011-9397-4.
- 972 Efroimsky, M. (2015), Tidal evolution of asteroidal binaries. ruled by viscosity. ignorant
 973 of rigidity, *The Astronomical Journal*, *150*(4), 98.
- 974 Efroimsky, M., and V. Lainey (2007), Physics of bodily tides in terrestrial planets and the
 975 appropriate scales of dynamical evolution, *Journal of Geophysical Research (Planets)*,
 976 *112*(E11), E12003, doi:10.1029/2007JE002908.

- 977 Efroimsky, M., and V. V. Makarov (2013), Tidal Friction and Tidal Lagging. Applicability
978 Limitations of a Popular Formula for the Tidal Torque, *apj*, 764, 26, doi:10.1088/0004-
979 637X/764/1/26.
- 980 Efroimsky, M., and V. V. Makarov (2014), Tidal dissipation in a homogeneous spherical
981 body. i. methods, *The Astrophysical Journal*, 795(1), 6.
- 982 Faul, U., and I. Jackson (2015), Transient creep and strain energy dissipation: An exper-
983 imental perspective, *Annual Review of Earth and Planetary Sciences*, 43, 541–569, doi:
984 10.1146/annurev-earth-060313-054732.
- 985 Findley, L., and K. Onaran (1965), *Creep and Relaxation of Nonlinear Viscoelastic Materi-*
986 *als*, Dover Publications, New York.
- 987 Folkner, W. M., V. Dehant, S. Le Maistre, M. Yseboodt, A. Rivoldini, T. Van Hoolst,
988 S. W. Asmar, and M. P. Golombek (2018), The rotation and interior structure experi-
989 ment on the insight mission to mars, *Space Science Reviews*, 214(5), 100.
- 990 Forte, A. M., and J. X. Mitrovica (2001), Deep-mantle high-viscosity flow and thermo-
991 chemical structure inferred from seismic and geodynamic data, *nature*, 410, 1049–1056.
- 992 Genova, A., S. Goossens, F. G. Lemoine, E. Mazarico, G. A. Neumann, D. E. Smith, and
993 M. T. Zuber (2016), Seasonal and static gravity field of Mars from MGS, Mars Odyssey
994 and MRO radio science, *icarus*, 272, 228–245, doi:10.1016/j.icarus.2016.02.050.
- 995 Gribb, T. T., and R. F. Cooper (1998), Low-frequency shear attenuation in polycrystalline
996 olivine: Grain boundary diffusion and the physical significance of the andrade model
997 for viscoelastic rheology, *Journal of Geophysical Research: Solid Earth*, 103(B11),
998 27,267–27,279.
- 999 Harada, Y., S. Goossens, K. Matsumoto, J. Yan, J. Ping, H. Noda, and J. Haruyama
1000 (2014), Strong tidal heating in an ultralow-viscosity zone at the core-mantle boundary
1001 of the Moon, *Nature Geoscience*, 7, 569–572, doi:10.1038/ngeo2211.
- 1002 Hauck, S. A., J.-L. Margot, S. C. Solomon, R. J. Phillips, C. L. Johnson, F. G. Lemoine,
1003 E. Mazarico, T. J. McCoy, S. Padovan, S. J. Peale, et al. (2013), The curious case of
1004 mercury’s internal structure, *Journal of Geophysical Research: Planets*, 118(6), 1204–
1005 1220.
- 1006 Helffrich, G. (2017), Mars core structure—concise review and anticipated insights from
1007 insight, *Progress in Earth and Planetary Science*, 4(1), 24, doi:10.1186/s40645-017-
1008 0139-4.

- 1009 Henning, W. G., R. J. O'Connell, and D. D. Sasselov (2009), Tidally heated terrestrial
1010 exoplanets: viscoelastic response models, *The Astrophysical Journal*, *707*(2), 1000.
- 1011 Hussmann, H., and T. Spohn (2004), Thermal-orbital evolution of io and europa, *Icarus*,
1012 *171*(2), 391 – 410, doi:<https://doi.org/10.1016/j.icarus.2004.05.020>.
- 1013 Jackson, I., and U. H. Faul (2010), Grainsize-sensitive viscoelastic relaxation in olivine:
1014 Towards a robust laboratory-based model for seismological application, *Physics of the*
1015 *Earth and Planetary Interiors*, *183*, 151–163, doi:10.1016/j.pepi.2010.09.005.
- 1016 Jackson, I., J. D. Fitz Gerald, U. H. Faul, and B. H. Tan (2002), Grain-size-sensitive seis-
1017 mic wave attenuation in polycrystalline olivine, *Journal of Geophysical Research: Solid*
1018 *Earth*, *107*(B12), ECV 5–1–ECV 5–16, doi:10.1029/2001JB001225, 2360.
- 1019 Jackson, I., U. H. Faul, J. D. F. Gerald, and B. H. Tan (2004), Shear wave attenuation and
1020 dispersion in melt-bearing olivine polycrystals: 1. specimen fabrication and mechanical
1021 testing, *Journal of Geophysical Research: Solid Earth*, *109*(B6).
- 1022 Jackson, I., et al. (2007), Properties of rock and minerals-physical origins of anelasticity
1023 and attenuation in rock, in *Treatise on geophysics*, Elsevier.
- 1024 Kamata, S., J. Kimura, K. Matsumoto, F. Nimmo, K. Kuramoto, and N. Namiki (2016),
1025 Tidal deformation of Ganymede: Sensitivity of Love numbers on the interior structure,
1026 *Journal of Geophysical Research (Planets)*, *121*, 1362–1375, doi:10.1002/2016JE005071.
- 1027 Karato, S., and H. A. Spetzler (1990), Defect microdynamics in minerals and solid-state
1028 mechanisms of seismic wave attenuation and velocity dispersion in the mantle, *Reviews*
1029 *of Geophysics*, *28*(4), 399–421, doi:10.1029/RG028i004p00399.
- 1030 Karato, S.-I. (1984), Grain-size distribution and rheology of the upper mantle, *Tectono-*
1031 *physics*, *104*(1-2), 155–176.
- 1032 Karato, S. I. (2008), *Deformation of Earth Materials*, Cambridge University Press.
- 1033 Karato, S.-i. (2013), Geophysical constraints on the water content of the lunar mantle and
1034 its implications for the origin of the Moon, *Earth and Planetary Science Letters*, *384*,
1035 144–153, doi:10.1016/j.epsl.2013.10.001.
- 1036 Karato, S.-i., T. Ologboji, and J. Park (2015), Mechanisms and geologic significance of
1037 the mid-lithosphere discontinuity in the continents, *Nature geoscience*, *8*(7), 509.
- 1038 Khan, A., and J. A. D. Connolly (2008), Constraining the composition and thermal state
1039 of Mars from inversion of geophysical data, *Journal of Geophysical Research (Planets)*,
1040 *113*, E07003, doi:10.1029/2007JE002996.

- 1041 Khan, A., C. Liebske, A. Rozel, A. Rivoldini, F. Nimmo, J. A. D. Connolly, A. Plesa, and
1042 D. Giardini (2018), A geophysical perspective on the bulk composition of mars, *Journal*
1043 *of Geophysical Research: Planets*, 123(2), 575–611, doi:10.1002/2017JE005371.
- 1044 Konopliv, A. S., and C. F. Yoder (1996), Venusian k2 tidal love number from magel-
1045 lan and pvo tracking data, *Geophysical Research Letters*, 23(14), 1857–1860, doi:
1046 10.1029/96GL01589.
- 1047 Konopliv, A. S., R. S. Park, and W. M. Folkner (2016), An improved JPL Mars gravity
1048 field and orientation from Mars orbiter and lander tracking data, *icarus*, 274, 253–260,
1049 doi:10.1016/j.icarus.2016.02.052.
- 1050 Lainey, V., V. Dehant, and M. Pätzold (2007), First numerical ephemerides of the Martian
1051 moons, *Astronomy and Astrophysics*, 465, 1075–1084, doi:10.1051/0004-6361:20065466.
- 1052 Lau, H. C., and U. H. Faul (2019), Anelasticity from seismic to tidal timescales: Theory
1053 and observations, *Earth and Planetary Science Letters*, 508, 18–29.
- 1054 Lau, H. C., U. Faul, J. X. Mitrovica, D. Al-Attar, J. Tromp, and G. Garapic (2016),
1055 Anelasticity across seismic to tidal timescales: a self-consistent approach, *Geophysical*
1056 *Journal International*, 208(1), 368–384, doi:10.1093/gji/ggw401.
- 1057 Lodders, K., and B. Fegley (1997), An Oxygen Isotope Model for the Composition of
1058 Mars, *icarus*, 126, 373–394, doi:10.1006/icar.1996.5653.
- 1059 Lognonné, P., and B. Mosser (1993), Planetary seismology, *Surveys in Geophysics*, 14,
1060 239–302, doi:10.1007/BF00690946.
- 1061 Lognonné, P., J. G. Beyneix, W. B. Banerdt, S. Cacho, J. F. Karczewski, and M. Morand
1062 (1996), Ultra broad band seismology on InterMarsNet, *Planets and Space Science*, 44,
1063 1237, doi:10.1016/S0032-0633(96)00083-9.
- 1064 Lognonné, P. e. a. (2019), Seis: Insight’s seismic experiment for internal structure of mars,
1065 *Space Science Reviews*, 215(1), 12, doi:10.1007/s11214-018-0574-6.
- 1066 McCarthy, C., and J. C. Castillo-Rogez (2013), Planetary ices attenuation properties, in
1067 *The Science of Solar System Ices*, pp. 183–225, Springer.
- 1068 McCarthy, C., Y. Takei, and T. Hiraga (2011), Experimental study of attenuation and
1069 dispersion over a broad frequency range: 2. the universal scaling of polycrystalline
1070 materials, *Journal of Geophysical Research: Solid Earth*, 116(B9), n/a–n/a, doi:
1071 10.1029/2011JB008384, b09207.
- 1072 McSween, H. Y., Jr., and S. M. McLennan (2014), Mars, in *Planets, Asteroids, Comets and*
1073 *The Solar System*, edited by K. Turekian and H. Holland, pp. 251–300, Elsevier Science,

- doi:10.1016/B978-0-08-095975-7.00125-X.
- 1074
1075 Minster, J. B., and D. L. Anderson (1981), A model of dislocation-controlled rheology for
1076 the mantle, *The Royal Society*, 299(1449), 319–356, doi:10.1098/rsta.1981.0025.
- 1077 Moczo, P., and J. Kristek (2005), On the rheological models used for time-domain
1078 methods of seismic wave propagation, *Geophysical Research Letters*, 32(1), doi:
1079 10.1029/2004GL021598.
- 1080 Moore, W. B., and G. Schubert (2000), NOTE: The Tidal Response of Europa, *icarus*,
1081 147, 317–319, doi:10.1006/icar.2000.6460.
- 1082 Morgan, J. W., and E. Anders (1979), Mars: a cosmochemical-geophysical estimate of
1083 bulk composition, in *Mars*, p. 60.
- 1084 Morris, S., and I. Jackson (2009), Implications of the similarity principle relating creep
1085 and attenuation in finely grained solids, *Materials Science and Engineering: A*, 521,
1086 124–127.
- 1087 Mosegaard, K., and A. Tarantola (1995), Monte carlo sampling of solutions to inverse
1088 problems, *Journal of Geophysical Research: Solid Earth (1978–2012)*, 100(B7), 12,431–
1089 12,447.
- 1090 Nimmo, F., and U. Faul (2013), Dissipation at tidal and seismic frequencies in a melt-free,
1091 anhydrous mars, *Journal of Geophysical Research: Planets*, 118(12), 2558–2569.
- 1092 Nimmo, F., U. H. Faul, and E. J. Garnero (2012), Dissipation at tidal and seismic frequen-
1093 cies in a melt-free Moon, *Journal of Geophysical Research (Planets)*, 117, E09005, doi:
1094 10.1029/2012JE004160.
- 1095 Nowick, A. S., and B. Berry (1972), *Anelastic relaxation in crystalline solids*, Academic
1096 Press.
- 1097 Padovan, S., J. Margot, S. A. Hauck, W. B. Moore, and S. C. Solomon (2013), The tides
1098 of mercury and possible implications for its interior structure, *Journal of Geophysical
1099 Research: Planets*, 119(4), 850–866, doi:10.1002/2013JE004459.
- 1100 Peale, S. (1977), Rotation histories of the natural satellites, in *IAU Colloq. 28: Planetary
1101 Satellites*, pp. 87–111.
- 1102 Peltier, W. (1974), The impulse response of a maxwell earth, *Reviews of Geophysics*,
1103 12(4), 649–669.
- 1104 Plesa, A.-C., M. Grott, N. Tosi, D. Breuer, T. Spohn, and M. A. Wieczorek (2016), How
1105 large are present-day heat flux variations across the surface of Mars?, *Journal of Geo-
1106 physical Research (Planets)*, 121, 2386–2403, doi:10.1002/2016JE005126.

- 1107 Pou, L., D. Mimoun, P. Lognonne, R. F. Garcia, O. Karatekin, M. Nonon-Latapie, and
1108 R. Llorca-Cejudo (2018), High precision seis calibration for the insight mission and its
1109 applications, *Space Science Reviews*, 215(1), 6, doi:10.1007/s11214-018-0561-y.
- 1110 Qin, C., S. Zhong, and J. Wahr (2016), Elastic tidal response of a laterally heterogeneous
1111 planet: a complete perturbation formulation, *Geophysical Journal International*, 207(1),
1112 89–110.
- 1113 Raj, R., and M. Ashby (1975), Intergranular fracture at elevated temperature, *Acta Metal-*
1114 *lurgica*, 23(6), 653–666.
- 1115 Ranalli, G. (2001), Mantle rheology: radial and lateral viscosity variations inferred
1116 from microphysical creep laws, *Journal of Geodynamics*, 32(4), 425 – 444, doi:
1117 [https://doi.org/10.1016/S0264-3707\(01\)00042-4](https://doi.org/10.1016/S0264-3707(01)00042-4).
- 1118 Remus, F., S. Mathis, J.-P. Zahn, and V. Lainey (2012), Anelastic tidal dissipation in
1119 multi-layer planets, *Astronomy & Astrophysics*, 541, A165.
- 1120 Renaud, J. P., and W. G. Henning (2018), Increased tidal dissipation using advanced rhe-
1121 ological models: Implications for io and tidally active exoplanets, *The Astrophysical*
1122 *Journal*, 857(2), 98.
- 1123 Rivoldini, A., T. Van Hoolst, O. Verhoeven, A. Mocquet, and V. Dehant (2011), Geodesy
1124 constraints on the interior structure and composition of Mars, *Icarus*, 213, 451–472,
1125 doi:10.1016/j.icarus.2011.03.024.
- 1126 Roberts, J. H., and F. Nimmo (2008), Tidal heating and the long-term stability of a sub-
1127 surface ocean on Enceladus, *icarus*, 194, 675–689, doi:10.1016/j.icarus.2007.11.010.
- 1128 Robuchon, G., G. Choblet, G. Tobie, O. Čadek, C. Sotin, and O. Grasset (2010), Coupling
1129 of thermal evolution and despinning of early iapetus, *Icarus*, 207(2), 959–971.
- 1130 Rosenblatt, P., S. Charnoz, K. M. Dunseath, M. Terao-Dunseath, A. Trinh, R. Hyodo,
1131 H. Genda, and S. Toupin (2016), Accretion of phobos and deimos in an extended de-
1132 bris disc stirred by transient moons, *Nature Geoscience*, 9(8), 581.
- 1133 Rozel, A. (2012), Impact of grain size on the convection of terrestrial planets, *Geochem-*
1134 *istry, Geophysics, Geosystems*, 13(10), doi:10.1029/2012GC004282.
- 1135 Ruedas, T., P. J. Tackley, and S. C. Solomon (2013), Thermal and compositional evolution
1136 of the martian mantle: Effects of phase transitions and melting, *Physics of the Earth and*
1137 *Planetary Interiors*, 216, 32–58, doi:10.1016/j.pepi.2012.12.002.
- 1138 Sanloup, C., A. Jambon, and P. Gillet (1999), A simple chondritic model of Mars, *Physics*
1139 *of the Earth and Planetary Interiors*, 112, 43–54, doi:10.1016/S0031-9201(98)00175-7.

- 1140 Sasaki, Y., Y. Takei, C. McCarthy, and J. F. Rudge (2019), Experimental study of disloca-
1141 tion damping using a rock analogue, *Journal of Geophysical Research: Solid Earth*.
- 1142 Seidelmann, P. K., V. K. Abalakin, M. Bursa, M. E. Davies, C. de Bergh, J. H. Lieske,
1143 J. Oberst, J. L. Simon, E. M. Standish, P. Stooke, and P. C. Thomas (2002), Report of
1144 the iau/iag working group on cartographic coordinates and rotational elements of the
1145 planets and satellites: 2000, *Celestial Mechanics and Dynamical Astronomy*, 82(1), 83–
1146 111, doi:10.1023/A:1013939327465.
- 1147 Smrekar, S. E., P. Lognonné, T. Spohn, W. B. Banerdt, D. Breuer, U. Christensen, V. De-
1148 hant, M. Drilleau, W. Folkner, N. Fuji, et al. (2019), Pre-mission insights on the interior
1149 of mars, *Space Science Reviews*, 215(1), 3.
- 1150 Sohl, F., G. Schubert, and T. Spohn (2005), Geophysical constraints on the composi-
1151 tion and structure of the Martian interior, *Journal of Geophysical Research (Planets)*,
1152 110(E9), E12008, doi:10.1029/2005JE002520.
- 1153 Soldati, G., L. Boschi, F. Deschamps, and D. Giardini (2009), Inferring radial models of
1154 mantle viscosity from gravity (GRACE) data and an evolutionary algorithm, *Physics of
1155 the Earth and Planetary Interiors*, 176, 19–32, doi:10.1016/j.pepi.2009.03.013.
- 1156 Stevenson, D. J. (2001), Mars' core and magnetism, *nature*, 412, 214–219.
- 1157 Stewart, A. J., M. W. Schmidt, W. van Westrenen, and C. Lieske (2007), Mars: A New
1158 Core-Crystallization Regime, *Science*, 316, 1323, doi:10.1126/science.1140549.
- 1159 Stixrude, L., and C. Lithgow-Bertelloni (2005b), Mineralogy and elasticity of the oceanic
1160 upper mantle: Origin of the low-velocity zone, *Journal of Geophysical Research: Solid
1161 Earth*, 110(B3), doi:10.1029/2004JB002965, b03204.
- 1162 Stixrude, L., and C. Lithgow-Bertelloni (2011), Thermodynamics of mantle miner-
1163 als - II. Phase equilibria, *Geophysical Journal International*, 184, 1180–1213, doi:
1164 10.1111/j.1365-246X.2010.04890.x.
- 1165 Sundberg, M., and R. Cooper (2010), A composite viscoelastic model for incorporating
1166 grain boundary sliding and transient diffusion creep; correlating creep and attenuation
1167 responses for materials with a fine grain size, *Philosophical Magazine*, 90(20), 2817–
1168 2840, doi:10.1080/14786431003746656.
- 1169 Takei, Y. (2017), Effects of partial melting on seismic velocity and attenuation: A new
1170 insight from experiments, *Annual Review of Earth and Planetary Sciences*, 45(1), null,
1171 doi:10.1146/annurev-earth-063016-015820.

- 1172 Takei, Y., F. Karasawa, and H. Yamauchi (2014), Temperature, grain size, and chemical
1173 controls on polycrystal anelasticity over a broad frequency range extending into the
1174 seismic range, *Journal of Geophysical Research: Solid Earth*, *119*(7), 5414–5443, doi:
1175 10.1002/2014JB011146.
- 1176 Taylor, G. J. (2013), The bulk composition of mars, *Chemie Der Erde-Geochemistry*,
1177 *73*(4), 401–420.
- 1178 Taylor, S. R., and S. McLennan (2008), *Planetary Crusts: Their Composition, Ori-*
1179 *gin and Evolution*, Cambridge Planetary Science, Cambridge University Press, doi:
1180 10.1017/CBO9780511575358.
- 1181 Tromp, J., and J. X. Mitrovica (1999), Surface loading of a viscoelastic earth-I. Gen-
1182 eral theory, *Geophysical Journal International*, *137*, 847–855, doi:10.1046/j.1365-
1183 246X.1999.00838.x.
- 1184 Van Hoolst, T., V. Dehant, F. Roosbeek, and P. Lognonné (2003), Tidally induced surface
1185 displacements, external potential variations, and gravity variations on Mars, *Icarus*, *161*,
1186 281–296, doi:10.1016/S0019-1035(02)00045-3.
- 1187 van Thienen, P., A. Rivoldini, T. Van Hoolst, and P. Lognonné (2006), A top-down origin
1188 for martian mantle plumes, *icarus*, *185*, 197–210, doi:10.1016/j.icarus.2006.06.008.
- 1189 Wahr, J., Z. A. Selvans, M. E. Mullen, A. C. Barr, G. C. Collins, M. M. Selvans, and
1190 R. T. Pappalardo (2009), Modeling stresses on satellites due to nonsynchronous rota-
1191 tion and orbital eccentricity using gravitational potential theory, *icarus*, *200*, 188–206,
1192 doi:10.1016/j.icarus.2008.11.002.
- 1193 Williams, J. G., and D. H. Boggs (2015), Tides on the Moon: Theory and determina-
1194 tion of dissipation, *Journal of Geophysical Research (Planets)*, *120*, 689–724, doi:
1195 10.1002/2014JE004755.
- 1196 Williams, J. G., S. G. Turyshev, D. H. Boggs, and J. T. Ratcliff (2006), Lunar laser rang-
1197 ing science: gravitational physics and lunar interior and geodesy, *Advances in Space*
1198 *Research*, *37*(1), 67–71.
- 1199 Williams, J. G., A. S. Konopliv, D. H. Boggs, R. S. Park, D.-N. Yuan, F. G. Lemoine,
1200 S. Goossens, E. Mazarico, F. Nimmo, R. C. Weber, S. W. Asmar, H. J. Melosh,
1201 G. A. Neumann, R. J. Phillips, D. E. Smith, S. C. Solomon, M. M. Watkins, M. A.
1202 Wiczorek, J. C. Andrews-Hanna, J. W. Head, W. S. Kiefer, I. Matsuyama, P. J. Mc-
1203 Govern, G. J. Taylor, and M. T. Zuber (2014), Lunar interior properties from the
1204 GRAIL mission, *Journal of Geophysical Research (Planets)*, *119*, 1546–1578, doi:

1205 10.1002/2013JE004559.

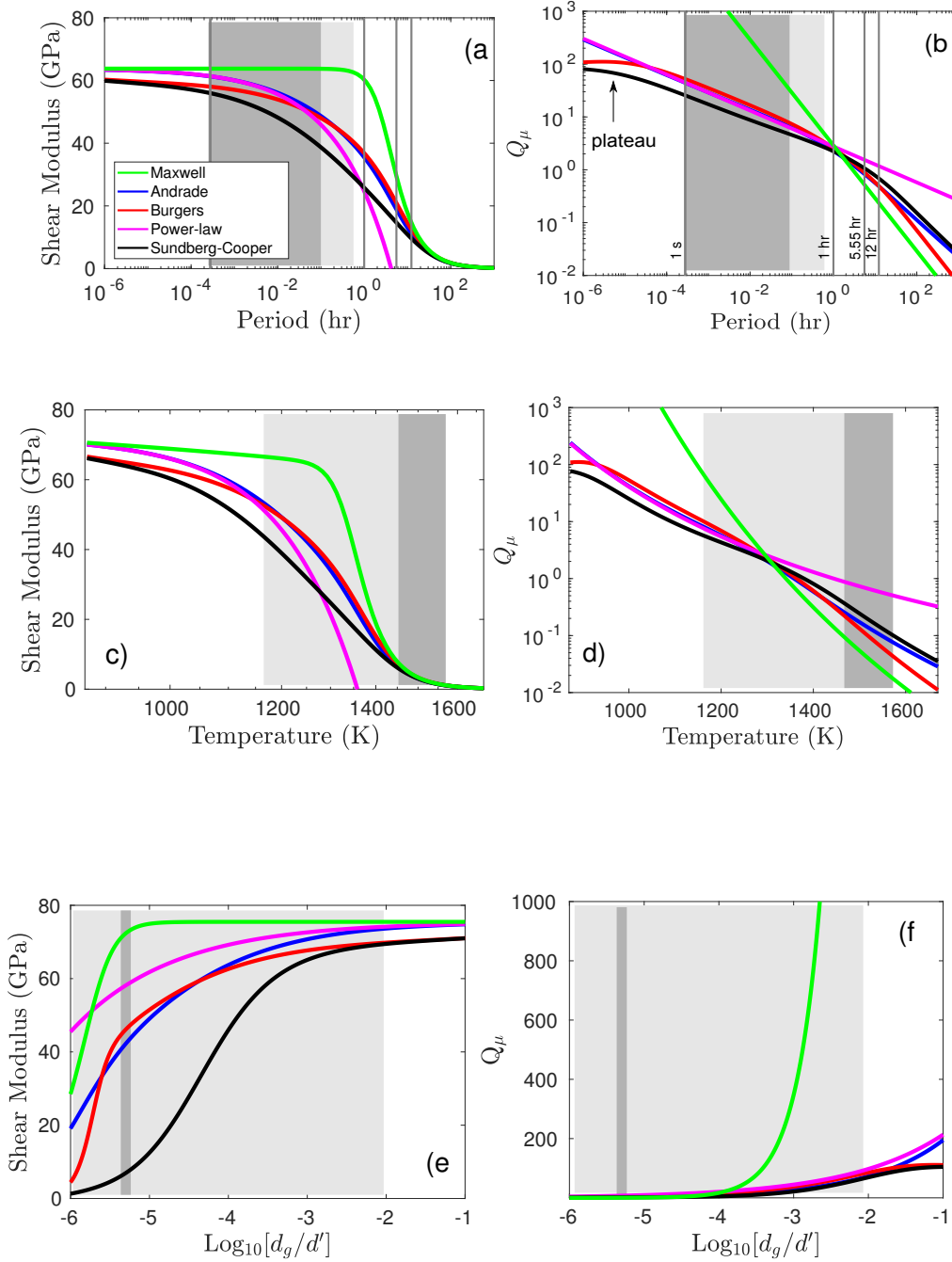
1206 Yoder, C. F. (1995), Venus' free obliquity, *Icarus*, *117*(2), 250–286.

1207 Yoder, C. F., A. S. Konopliv, D. N. Yuan, E. M. Standish, and W. M. Folkner (2003),
1208 Fluid Core Size of Mars from Detection of the Solar Tide, *Science*, *300*, 299–303, doi:
1209 10.1126/science.1079645.

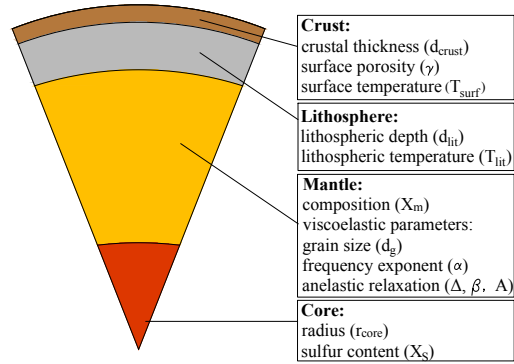
1210 Zharkov, V. N., and T. V. Gudkova (1997), On the dissipative factor of the Martian interi-
1211 ors, *Planets and Space Science*, *45*, 401–407, doi:10.1016/S0032-0633(96)00144-4.

1212 Zharkov, V. N., and T. V. Gudkova (2005), Construction of Martian Interior Model, *Solar*
1213 *System Research*, *39*, 343–373, doi:10.1007/s11208-005-0049-7.

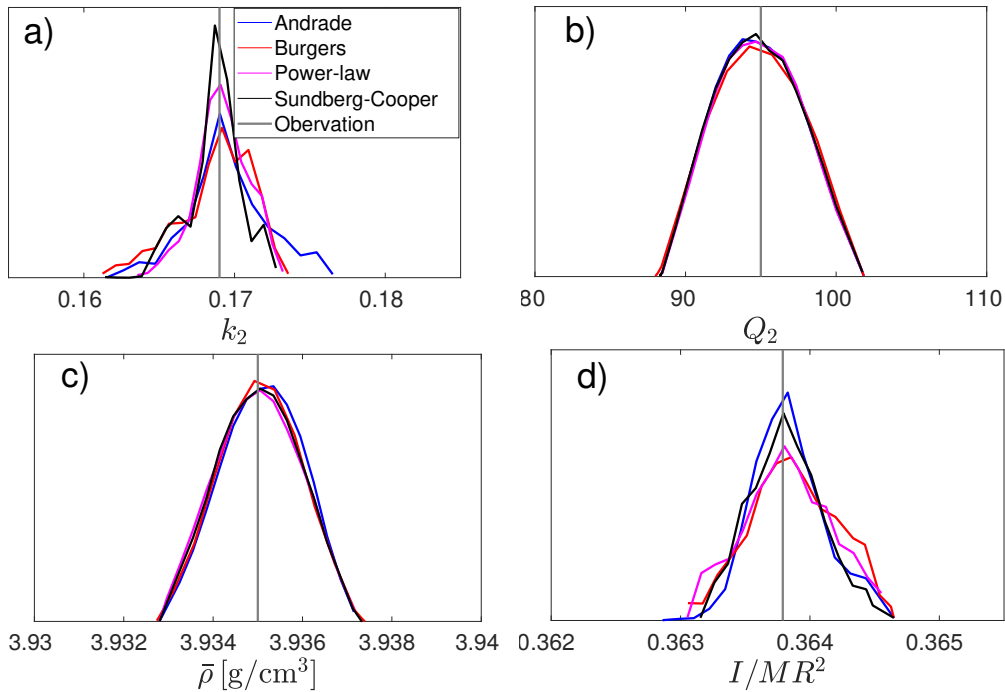
1214 Zharkov, V. N., and T. V. Gudkova (2009), The period and Q of the Chandler wobble of
1215 Mars, *planss*, *57*, 288–295, doi:10.1016/j.pss.2008.11.010.



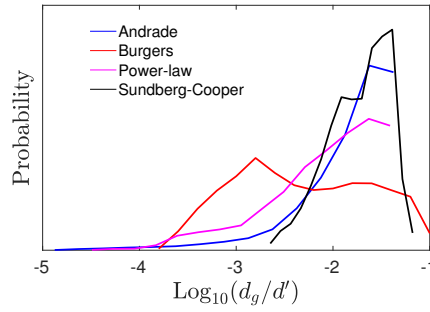
418 **Figure 3.** Computed variations of relaxed shear modulus (G_R) and shear attenuation (Q_μ) with period,
 419 temperature, and grain size for the five rheological models considered in this study. (a, b) G_R and Q_μ a
 420 function of period at constant temperature and grain size, The vertical lines show periods of interest: seismic
 421 body waves (1 s), normal modes (1 hr), main tidal excitation of Phobos (5.55 hr), and main tidal excitation
 422 of the Sun (12.32 hr). (c, d) G_R and Q_μ as a function of temperature at constant period and grain size, (e, f)
 423 G_R and Q_μ as a function of grain size at constant period and temperature. Light and dark shaded areas denote
 424 the ranges covered by the experimental measurements of *Jackson and Faul* [2010] and *Sundberg and Cooper*
 425 [2010], respectively. All curves were produced at a constant pressure of 10.4 GPa and for an unrelaxed shear
 426 modulus of 65 GPa. Viscoelastic parameter values employed are given in Table A.1 and $d' = 1$ m.



477 **Figure 4.** Schematic diagram illustrating model parameterization. The model is spherically symmetric and
 478 divided into crust, lithosphere, mantle, and core. These four layers are parameterized using the parameters
 479 shown in the boxes on the right. For more details see main text (section 4.1).

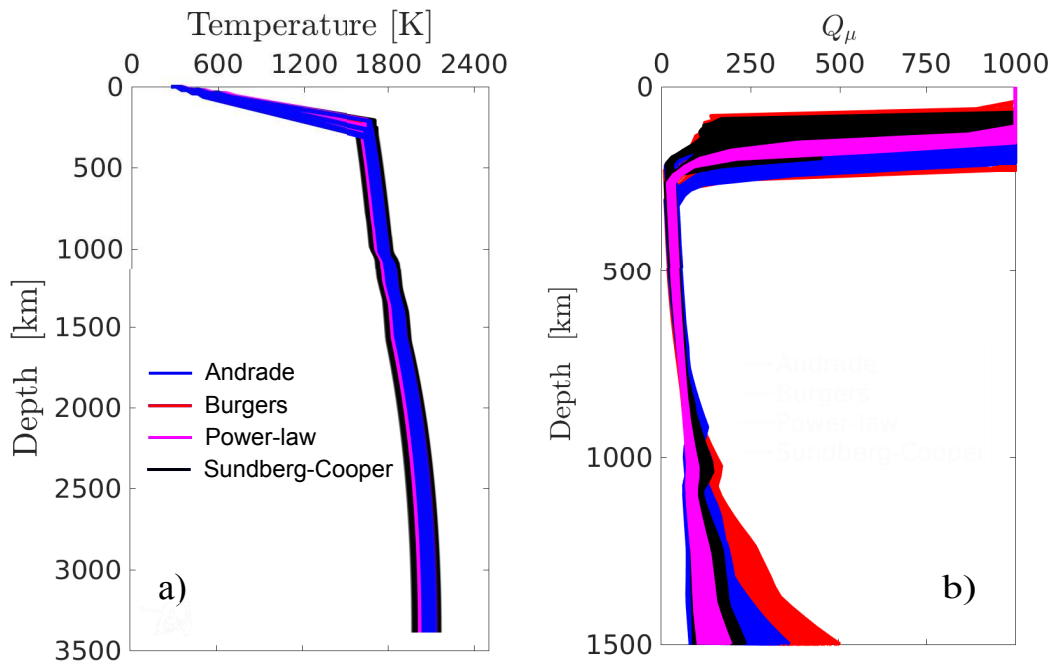


559 **Figure 5.** Computed data distributions showing fit to observations for each of the rheological models: a)
 560 second-degree tidal Love number k_2 ; b) second-degree global tidal dissipation Q_2 ; c) mean density $\bar{\rho}$; and
 561 d) mean moment of inertia I/MR^2 . The results shown in (a) and (b) refer to the main tidal period of Phobos.
 562 The vertical solid lines indicate observed values of k_2 , Q_2 , $\bar{\rho}$, and I/MR^2 . Observations and uncertainties are
 563 compiled in table 1.



589

Figure 6. Sampled distributions of grain-size for each viscoelastic model obtained from the inversion.



709

Figure 7. Inverted areothermal (a) and shear attenuation (b) profiles for the main viscoelastic models con-

710

sidered in this study (at the main tidal period of Phobos). Shear attenuation models are only shown down to

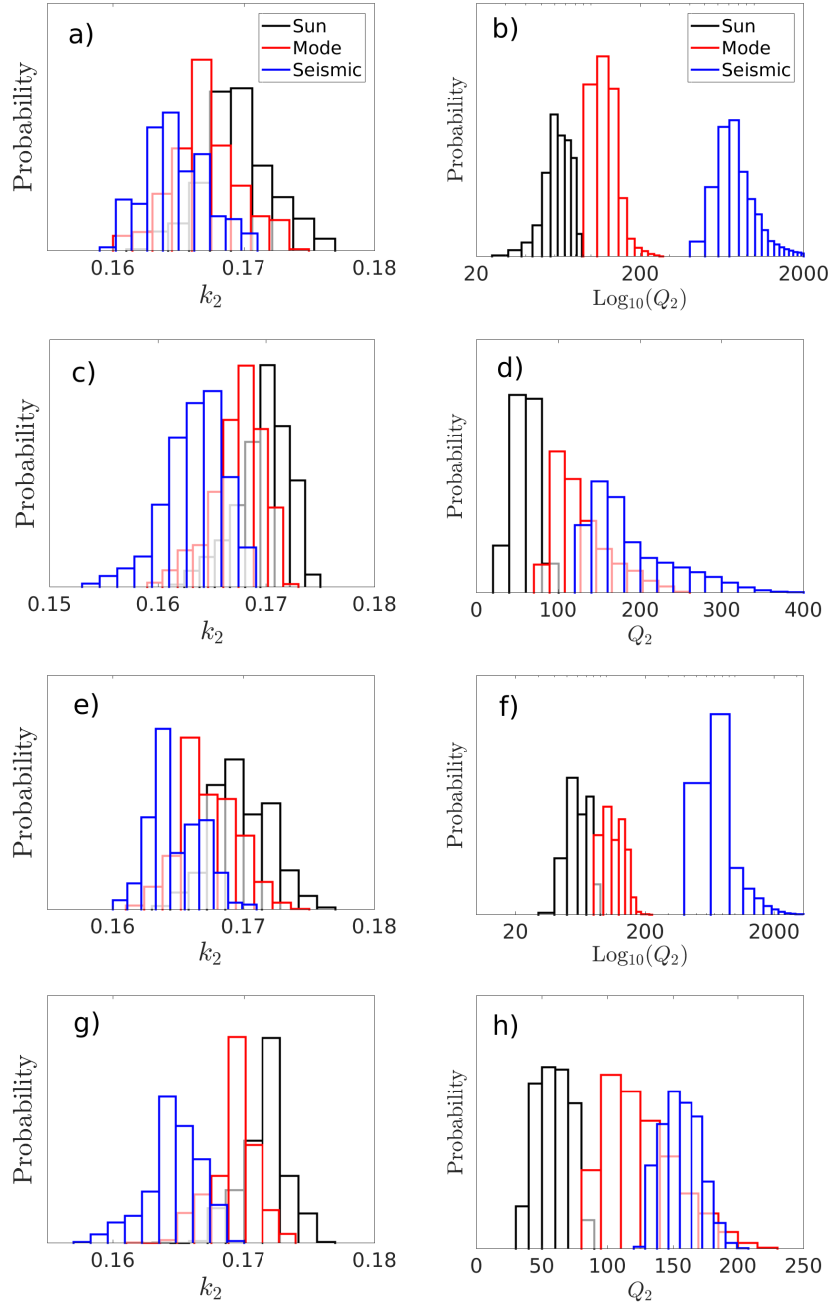
711

the core-mantle-boundary since the core is fluid ($Q_{\mu}=0$).

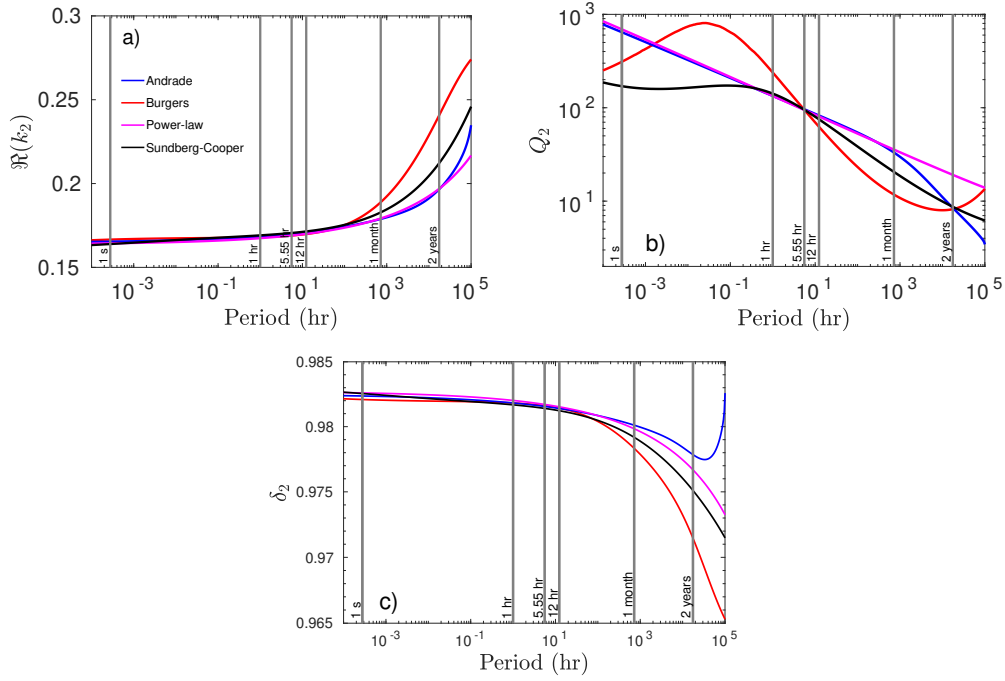
| | Andrade | | | Burgers | | | Power-law | | | Sundberg-Cooper | | |
|------------|---------|--------|--------|---------|---------|--------|-----------|--------|---------|-----------------|--------|--------|
| | Seismic | Mode | Phobos | Solar | Seismic | Mode | Phobos | Solar | Seismic | Mode | Phobos | Solar |
| k_3 | 0.0505 | 0.051 | 0.052 | 0.0522 | 0.0505 | 0.0518 | 0.052 | 0.0522 | 0.051 | 0.051 | 0.052 | 0.0525 |
| k_4 | 0.0227 | 0.0232 | 0.0235 | 0.0244 | 0.0233 | 0.0239 | 0.024 | 0.0244 | 0.023 | 0.0235 | 0.0237 | 0.024 |
| k_5 | 0.0134 | 0.0137 | 0.0138 | 0.0145 | 0.0138 | 0.0142 | 0.0145 | 0.0145 | 0.0135 | 0.0138 | 0.0141 | 0.0143 |
| h_2 | 0.229 | 0.232 | 0.233 | 0.235 | 0.232 | 0.234 | 0.235 | 0.235 | 0.23 | 0.232 | 0.233 | 0.233 |
| h_3 | 0.103 | 0.105 | 0.105 | 0.106 | 0.105 | 0.106 | 0.106 | 0.106 | 0.103 | 0.105 | 0.105 | 0.105 |
| h_4 | 0.061 | 0.063 | 0.063 | 0.064 | 0.062 | 0.064 | 0.064 | 0.064 | 0.061 | 0.063 | 0.063 | 0.063 |
| h_5 | 0.045 | 0.046 | 0.046 | 0.046 | 0.046 | 0.048 | 0.048 | 0.048 | 0.045 | 0.046 | 0.046 | 0.046 |
| δ_2 | 0.9845 | 0.98 | 0.9795 | 0.978 | 0.9845 | 0.9805 | 0.98 | 0.98 | 0.984 | 0.98 | 0.978 | 0.978 |
| δ_3 | 1.001 | 1.002 | 1.002 | 1.001 | 1.003 | 1.002 | 1.001 | 1.001 | 1.001 | 1.002 | 1.001 | 1.000 |
| δ_4 | 1.002 | 1.003 | 1.002 | 1.002 | 1.002 | 1.002 | 1.002 | 1.002 | 1.002 | 1.002 | 1.002 | 1.002 |
| δ_5 | 1.006 | 1.006 | 1.006 | 1.006 | 1.006 | 1.006 | 1.006 | 1.006 | 1.006 | 1.006 | 1.005 | 1.005 |
| l_2 | 0.037 | 0.038 | 0.038 | 0.038 | 0.038 | 0.04 | 0.04 | 0.04 | 0.037 | 0.039 | 0.039 | 0.039 |
| l_3 | 0.0064 | 0.0066 | 0.0066 | 0.0066 | 0.0065 | 0.007 | 0.0073 | 0.0073 | 0.0064 | 0.0066 | 0.0067 | 0.0067 |
| l_4 | 0.003 | 0.003 | 0.003 | 0.003 | 0.003 | 0.003 | 0.003 | 0.003 | 0.003 | 0.003 | 0.003 | 0.003 |
| l_5 | 0.0018 | 0.0019 | 0.0019 | 0.0019 | 0.0019 | 0.002 | 0.002 | 0.002 | 0.00185 | 0.002 | 0.002 | 0.002 |
| Q_3 | 700 | 152 | 83 | 75 | 185 | 152 | 82 | 75 | 800 | 142 | 83 | 77 |
| Q_4 | 700 | 137 | 70 | 66 | 170 | 150 | 66 | 65 | 700 | 130 | 70 | 67 |
| Q_5 | 650 | 115 | 65 | 58 | 155 | 115 | 57 | 52 | 650 | 108 | 60 | 55 |

Table 6. Predicted tidal properties of Mars until spherical harmonic degree 5 based on the inversion results (mean values) for individual rheological models at four different periods:

seismic: 1 sec, Mode: 1 hr, Phobos: 5.55 hr, and Solar: 12.32 hr. Note that these periods are based on degree 2 and should be modified for higher degrees, i.e., $n=3, 4,$ and 5 correspond to forcing frequencies of 3.7, 2.775, and 2.22 hrs, respectively.



712 **Figure 8.** Sampled distributions of second-degree tidal Love number k_2 and quality factor Q_2 at three
 713 different periods of geophysical interest for each rheological model: a-b) Andrade, c-d) extended Burgers,
 714 e-f) power-law, and g-h) Sundberg-Cooper. Note that because of the large variation in Q_2 for the Andrade
 715 and power-law models, plots b) and f) are shown in terms of $\text{Log}_{10}(Q_2)$. The distributions represent predic-
 716 tions based on the observed 5.55-hr main Phobos tide. The periods considered are: 12.32 hr (solar tide), 1 hr
 717 (long-period normal modes), and 1 s (short-period body waves).



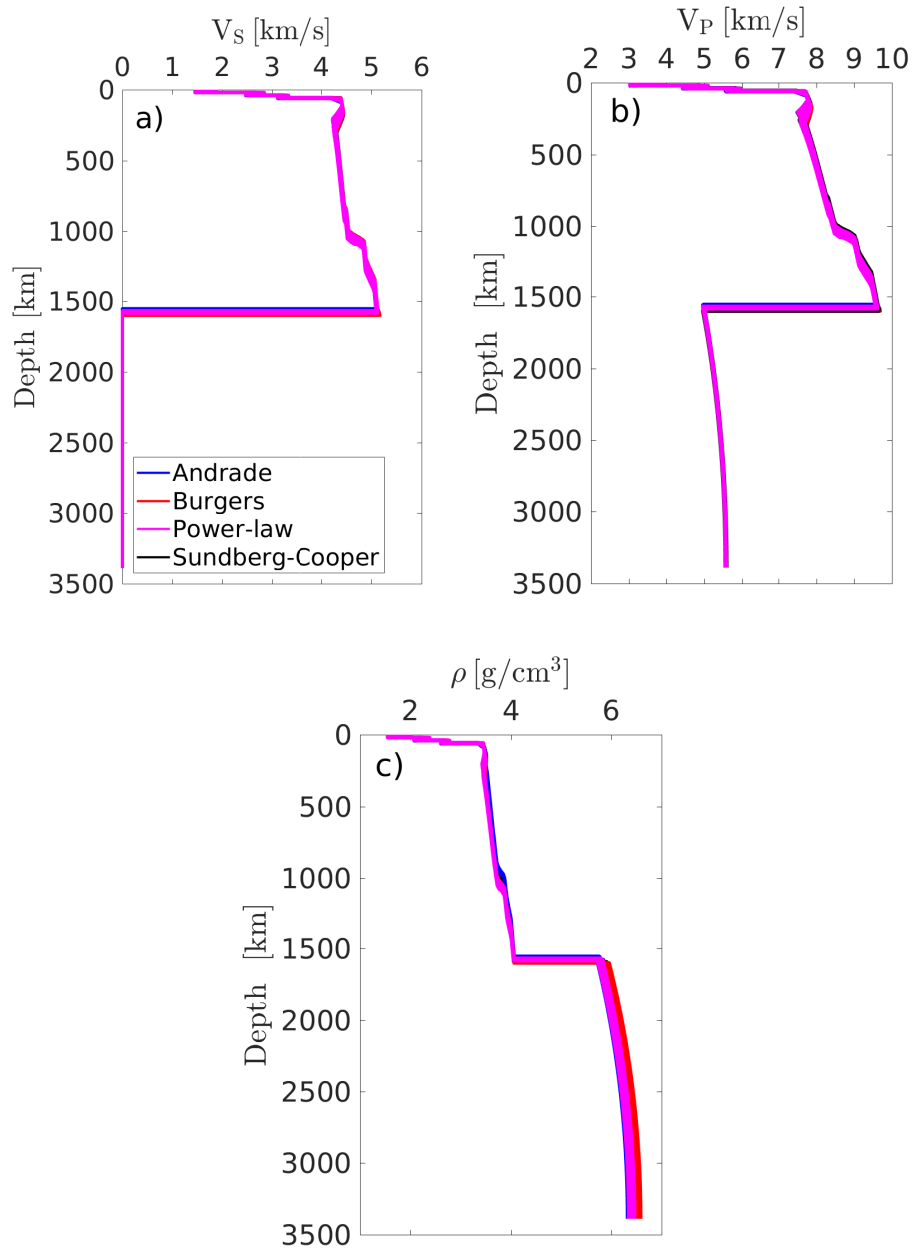
718 **Figure 9.** Computed tidal response of Mars as a function of period from short-period seismic (1 s) to long-
 719 period tidal time scales (~ 10 yr) for the four major rheological models considered in this study. a) Amplitude
 720 of tidal response (real part of second-degree potential Love number k_2), b) second-degree global tidal quality
 721 factor (Q_2), and c) gravimetric factor (δ_2). The response curves were computed using the maximum like-
 722 likelihood model obtained in the inversion and the viscoelastic parameters compiled in the Table A.1 for each
 723 rheology.

| Parameter | Unit | Andrade | Extended Burgers | Power-law | Sundberg-Cooper | Maxwell |
|--|------|-----------|------------------|-----------|-----------------|-------------------|
| Crustal thickness (T_{crust}) | km | 50–75 | 50–75 | 50–70 | 50–75 | 45–60 |
| Lithospheric depth (d_{lit}) | km | 225–350 | 225–340 | 225–300 | 225–325 | 180–350 |
| Lithospheric Temperature (T_{lit}) | K | 1650–1670 | 1650–1690 | 1640–1670 | 1630–1690 | 1560–1585 |
| CMB Temperature | K | 1830–1940 | 1860–1910 | 1830–1910 | 1780–1950 | 1930–1990 |
| Core radius (r_{core}) | km | 1790–1850 | 1750–1810 | 1790–1850 | 1760–1840 | 1830–1890 |
| Core sulfur content (X_S) | wt % | 18–19.5 | 17–19 | 18–19 | 17–19 | 19.5–20.5 |
| Viscosity (η) | Pa·s | – | – | – | – | $2 \cdot 10^{16}$ |

Table 7. Summary of inversion results for each of the rheological models considered in this study. Ranges indicate the 90% credible interval. CMB refers to the core-mantle-boundary.

| Parameter | Value | Unit | Viscoelastic model |
|-------------------------|----------------------|------------------------------------|--------------------|
| β | $3.2 \cdot 10^{-13}$ | $\text{Pa}^{-1} \text{ s}^{-0.33}$ | A |
| β | $0.5 \cdot 10^{-13}$ | $\text{Pa}^{-1} \text{ s}^{-0.33}$ | SC |
| Δ_B | 1.4 | – | ExtB, SC |
| α | 0.33 | – | all |
| A | 0.002 | $\text{s}^{-0.33}$ | PL |
| d_0 | 13.4 | μm | all |
| P_0 | 0.2 | GPa | all |
| T_0 | 1173 | K | all |
| τ_{L0} | 10^{-3} | s | ExtB, SC |
| τ_{H0} | 10^7 | s | ExtB, SC |
| τ_{M0} | $10^{7.48}$ | s | all |
| τ_{P0} | $10^{-3.4}$ | s | ExtB, SC |
| Δ_P | 0.057 | – | ExtB, SC |
| m_{ga} | 1.3 | – | A, M, ExtB, SC |
| m_{gv} | 3 | – | A, M, ExtB, SC |
| V^* | 10^{-5} | m^3/mol | all |
| E^* | 360 | kJ/mol | all |
| $\partial G/\partial P$ | 1.8 | – | all |
| $\partial G/\partial T$ | -13.6 | MPa/K | all |
| σ | 4 | – | ExtB, SC |

833 **Table A.1.** Compilation of viscoelastic parameters used in this study. Abbreviations are: A–Andrade;
834 ExtB–extended Burgers; M–Maxwell; PL–power-law; SC–Sundberg-Cooper. The values of $\partial G/\partial P$ and
835 $\partial G/\partial T$ are only employed for creating the models discussed in section 2.3. All parameter values used are
836 from *Jackson and Faul* [2010], except for β and A (SC and PL), which are based on forward model runs such
837 that the modeled Q_μ and G_R (shown in Figure 3) among the various rheologies have comparable amplitudes.



889 **Figure C.1.** Inverted seismic wave speed and density profiles obtained for each of the rheological models.

890 a) P-wave speed (V_P), b) S-wave speed (V_S), and c) density (ρ).